Quasi-3-D Seismic Reflection Imaging and Wide-Angle Velocity Structure of Nearly Amagmatic Oceanic Lithosphere at the Ultraslow-Spreading Southwest Indian Ridge

Ekeabino Momoh, Mathilde Cannat, Louise Watremez, Sylvie Leroy, Satish Singh

To cite this version:

Ekeabino Momoh, Mathilde Cannat, Louise Watremez, Sylvie Leroy, Satish Singh. Quasi-3-D Seismic Reflection Imaging and Wide-Angle Velocity Structure of Nearly Amagmatic Oceanic Lithosphere at the Ultraslow-Spreading Southwest Indian Ridge. Journal of Geophysical Research : Solid Earth, 2017, 122 (12), pp.9511-9533. ⟨10.1002/2017JB014754⟩. ⟨insu-01828219⟩

HAL Id: insu-01828219

https://insu.hal.science/insu-01828219v1

Submitted on 3 Jul 2018

AGU PUBLICATIONS

JGR

Journal of Geophysical Research: Solid Earth

RESEARCH ARTICLE

10.1002/2017JB014754

Key Points:
- First 3-D seismic reflection image on-axis in an end-member setting of mid-ocean ridge environment with nearly zero melt supply
- Active detachment fault proposed for mantle exhumation is imaged as a damaged zone down to 5 km below the seafloor dipping 45–60°
- Crustal thickness ranges between 4 and 5 km, probably representing the extent of fault damage zone and serpentinization

Supporting Information:
- Supporting Information S1
- Figure S1
- Figure S2
- Figure S3
- Figure S4
- Figure S5

Correspondence to:
E. Momoh,
momoh@ipgp.fr

Citation:
Momoh, E., Cannat, M., Watremez, L., Leroy, S., & Singh, S. C. (2017). Quasi-3-D seismic reflection imaging and wide-angle velocity structure of nearly amagmatic oceanic lithosphere at the ultraslow-spreading Southwest Indian Ridge. *Journal of Geophysical Research: Solid Earth*, *122*, 9511–9533. https://doi.org/10.1002/2017JB014754

Received 25 JUL 2017
Accepted 16 NOV 2017
Accepted article online 20 NOV 2017
Published online 13 DEC 2017
Corrected 16 APR 2018

This article was corrected on 16 APR 2018. See the end of the full text for details.

Quasi-3-D Seismic Reflection Imaging and Wide-Angle Velocity Structure of Nearly Amagmatic Oceanic Lithosphere at the Ultraslow-Spreading Southwest Indian Ridge

Ekeabino Momoh[1], **Mathilde Cannat**[1], **Louise Watremez**[2,3], **Sylvie Leroy**[2], **and Satish C. Singh**[1]

[1]Geoscience Marines, Institut de Physique du Globe de Paris, Paris, France, [2]ISTeP, UPMC, CNRS UMR 7193, Sorbonne Universités, Paris CEDEX 05, France, [3]Now at Université Lille, CNRS, Université Littoral Côte d'Opale, UMR 8187, LOG, Laboratoire d'Océanologie et de Géosciences, Lille, France

Abstract We present results from 3-D processing of 2-D seismic data shot along 100 m spaced profiles in a 1.8 km wide by 24 km long box during the SISMOSMOOTH 2014 cruise. The study is aimed at understanding the oceanic crust formed at an end-member mid-ocean ridge environment of nearly zero melt supply. Three distinct packages of reflectors are imaged: (1) south facing reflectors, which we propose correspond to the damage zone induced by the active axial detachment fault: reflectors in the damage zone have dips up to 60° and are visible down to 5 km below the seafloor; (2) series of north dipping reflectors in the hanging wall of the detachment fault: these reflectors may correspond to damage zone inherited from a previous, north dipping detachment fault, or small offset recent faults, conjugate from the active detachment fault, that served as conduits for isolated magmatic dykes; and (3) discontinuous but coherent flat-lying reflectors at shallow depths (<1.5 km below the seafloor), and at depths between 4 and 5 km below the seafloor. Comparing these deeper flat-lying reflectors with the wide-angle velocity model obtained from ocean-bottom seismometers data next to the 3-D box shows that they correspond to parts of the model with *P* wave velocity of 6.5–8 km/s, suggesting that they occur in the transition between lower crust and upper mantle. The 4–5 km layer with crustal *P* wave velocities is interpreted as primarily due to serpentinization and fracturation of the exhumed mantle-derived peridotites in the footwall of active and past detachment faults.

1. Introduction

Ultramafic outcrops observed on the seafloor at slow- and ultraslow-spreading ridges call for the need to understand the relative contributions of tectonic and magmatic processes to spreading, and the nature of the oceanic crust in such domains. Some examples of ultramafic exposures are outcrops of variably serpentinized peridotites observed with or without gabbros, forming so-called oceanic core complexes (OCCs) at the Mid-Atlantic Ridge (MAR) axial valley wall (e.g., Cannat, 1993; Cannat et al., 1997; Dick et al., 2008; Karson et al., 1987; Mével et al., 1991). Several studies attempt to explain the emplacement of these ultramafics on the seafloor, and the critical role of large offset normal faults ("detachment faults") exhuming lower crust and upper mantle rocks along their footwalls has been recognized (e.g., Cann et al., 1997; Cannat, 1993; Cannat et al., 1997; Dick et al., 1981; Escartín et al., 2008; Karson, 1990; MacLeod et al., 2002). Some active MAR detachment faults emerge at shallow angles (<20°) at the seafloor (Smith et al., 2006); however, current evidence from surface geology (e.g., MacLeod et al., 2009), paleomagnetic studies of reoriented core samples (e.g., Garcés & Gee, 2007; Morris et al., 2009), and numerical modeling (e.g., Buck, 1988; Lavier et al., 1999; Schouten et al., 2010; Tucholke et al., 2008) suggest that active detachment faults steepen at depth (>45°) and are rotated to shallower angles as the footwall is exhumed. This is supported by the distribution of microseismic events that outline a steeply dipping (~70°) fault domain down to, respectively, 7 km and 10 km below the seafloor at the Trans-Atlantic Geotraverse detachment fault (deMartin et al., 2007) and 13°20′N MAR (Parnell-Turner et al., 2017). Structures interpreted as former axial detachment faults have also been imaged seismically in Cretaceous MAR lithosphere showing relatively steep faults (30–45°) extending ~2 km in the basement (Reston & Ranero, 2011). The subseafloor portion of an active axial detachment faults has, however, not been imaged by seismic reflection techniques prior to the study reported here.

Oceanic core complexes can occur as domes bearing spreading-parallel undulations (corrugations; Cann et al., 1997). Areas of ultramafic exposure at the seafloor, interpreted as OCCs in a broad sense, also occur in domains that do not present corrugations, such as the smooth seafloor terranes of the easternmost Southwest Indian Ridge (SWIR) (Cannat et al., 2006). OCCs, which have been sampled by dredging, show a variety of petrologic compositions; for example, the occurrence of peridotites, gabbros, and volcanics has been reported at 13°N, 13°48′N, 15°45′N, 16°25′N, 26°35′N, and 23°30′N in the MAR (Picazo et al., 2012; MacLeod et al., 2009; Escartín et al., 2003, 2017; Smith et al., 2014; Tucholke et al., 2001; Dick et al., 2008, respectively); 25°S in the Central Indian Ridge (Sato et al., 2009); and 49°39′N at the Southwest Indian Ridge (SWIR) (Zhao et al., 2013). These suggest that the interplay between tectonic stretching and magmatic intrusion is likely at OCCs formed in these regions. Other OCCs sampled revealed that variably serpentinized peridotites are predominant, with minor gabbros, e.g., 36°14′N at the MAR (Andréani et al., 2014) and 13°E (Dick et al., 2003) and 64°E to 66°E at the SWIR (Cannat et al., 2006; Sauter et al., 2013). In this case, OCC formation likely occurred at near-zero melt supply.

To model the relative contribution of magmatic processes and tectonic extension to spreading at mid-ocean ridges, Buck et al. (2005) introduced the M factor, which takes account of the proportion of plate separation taken by normal faulting and magmatic dyking. For M near 0.5 (i.e., magmatic dyking taking about 50% of total plate separation), numerical models predict that faults should remain localized at the ridge axis and develop into large offset detachments. At $M < 0.5$, models have the fault moving with the hanging wall plate progressively outside the axial domain, a setting that eventually promotes the initiation of new faults that tend to flip polarity at near-zero melt supply (Tucholke et al., 2008).

The crustal thicknesses determined from wide-angle seismics at OCCs are thinner than the average crustal thickness of ~7 km observed at more magmatic domains in the MAR (White et al., 1992). The crustal thickness ranges between 4.5 and 6 km at the Atlantis Massif (30°N, MAR; Blackman & Collins, 2010) and 2.8–5 km along-axis at the rifted oceanic core complex at 5°S, MAR (Planert et al., 2010; Planert et al., 2009). The crustal thickness is 4 km below the dominantly gabbroic OCC revealed by Ocean Drilling Program (ODP) Hole 735B at Atlantis Bank, SWIR (Muller et al., 1997). At 62°E, SWIR, it is ~5 km thick (Minshull & White, 1996), while at 66°E, the estimated crustal thickness is 4.2 km on average (Minshull et al., 2006). Areas of ultramafic exposure at the easternmost SWIR and elsewhere along slow- and ultraslow-spreading ridges have also been correlated with higher Residual Mantle Bouguer Anomaly, which is consistent with thinner crust than the surrounding more volcanically robust areas (Cannat et al., 1995, 2006). The geophysically defined crust is therefore not absent in these areas, which is probably because of fracturation and hydrous alteration of the mantle-derived material, which consequently results in geophysical signatures that are similar in crustal geophysical properties, e.g., lower density and compressional (P) wave velocity (Christensen, 1972, 2004; Miller & Christensen, 1997). Most samples of peridotites from the MAR and SWIR are indeed extensively serpentinized and reveal tight networks of microfractures that served as channels for serpentinizing fluids (e.g., Früh-Green et al., 2004; Plümper et al., 2012; Rouméjon & Cannat, 2014). Oxygen isotope studies of serpentinized samples also help constrain the temperature conditions during serpentinization, which in most cases are found to be between 200°C and 350°C (Agrinier & Cannat, 1997; Bonatti, 1976; Früh-Green et al., 2004; Rouméjon et al., 2015). Two hypotheses have been proposed to account for the distribution of serpentinites in the oceanic lithosphere: one is the serpentinization front hypothesis where hydrothermal fluids percolate vertically downward in the crust as tensile stresses initiated by temperature differences between the hydrothermally cooled domain and hotter underlying rocks initiate cracks in the hotter rocks, thereby allowing the overlying fluids to penetrate further (Lister, 1974). The other hypothesis that is more recent proposes that serpentinization develops due to hydrothermal fluid circulation in the fractured footwall of axial detachments (Andréani et al., 2007; Cannat et al., 2010; Rouméjon & Cannat, 2014). In this second hypothesis, the thickness of the geophysically defined crust in areas of ultramafic exposures is therefore predicted to be related to the extent of detachment fault-related fracturation, i.e., damage induced by detachment faulting.

This paper provides active source seismic constraints on the thickness, seismic velocity, and reflectivity structure of the axial domain in a nearly amagmatic region of the ultraslow-spreading SWIR (14 mm/yr full rate (Patriat & Segoufin, 1988)). We analyze 2-D multichannel seismic reflection data using a 3-D processing workflow, and wide-angle seismic refraction data. From our data analyses, we address the geometry and internal structure of the active axial detachment fault, and how it may impact serpentinization.

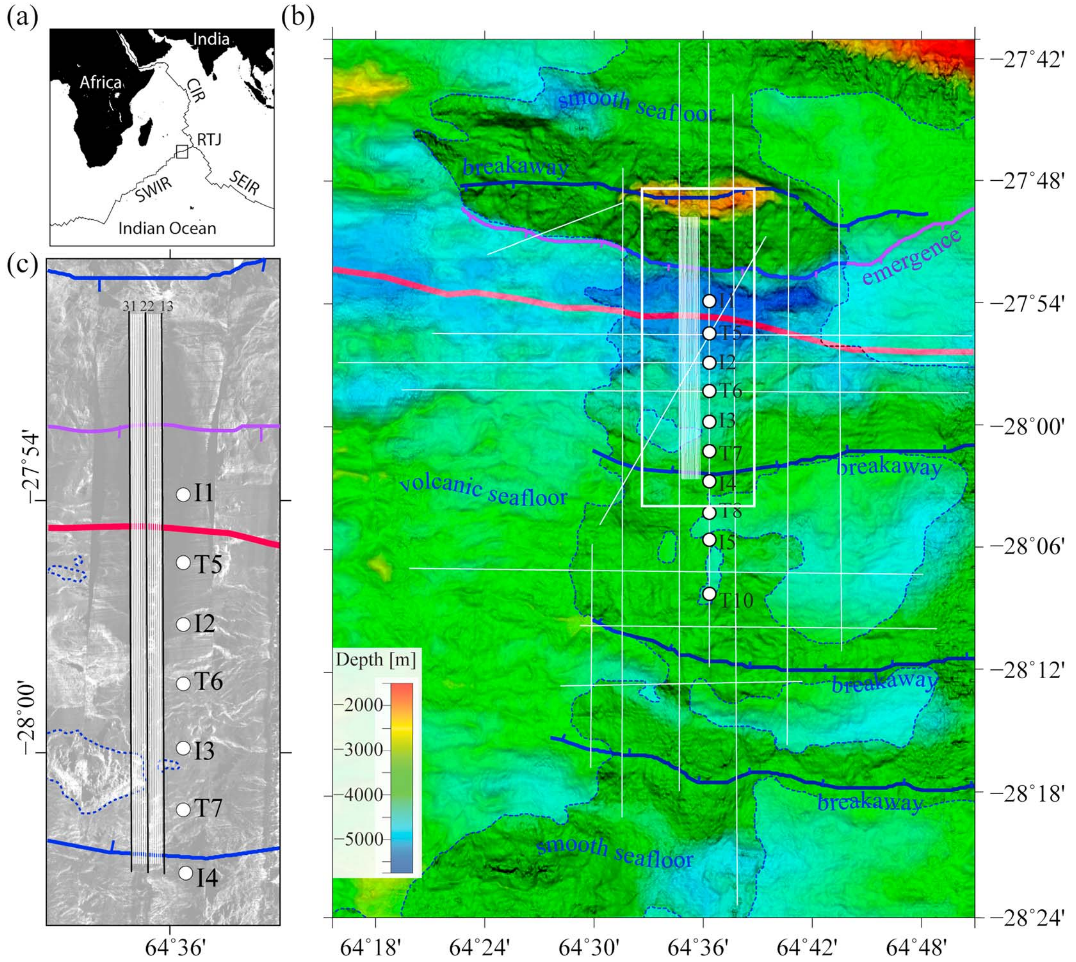

Figure 1. (a) Location of the study area at the Southwest Indian Ridge (SWIR, 64°E longitude). (b) Bathymetric map of the study area at the easternmost Southwest Indian Ridge showing the boundary between a corridor of nearly amagmatic smooth seafloor (dark shading on map) and volcanic seafloor (dashed blue line; Cannat et al., 2006). The breakaway of the inferred active axial detachment fault is mapped at the top of the northern axial valley wall, and its emergence is shown in purple (Sauter et al., 2013). Proposed inactive detachment fault breakaways are indicated in the southern Antarctic plate. These breakaways are drawn following the apex of successive ridge-parallel elongated massifs. The red thick line indicates the ridge axis (Sauter et al., 2013). The white rectangle indicates an area where the seafloor reflectivity was surveyed by a towed ocean-bottom instrument (Sauter et al., 2013), which is shown in Figure 1c. The thin white lines in the narrow box within the larger white rectangle show eighteen 2-D multichannel seismic lines, spaced by 100 m that we processed in a 3-D manner in this study. These lines are numbered 13 to 31 (from east to west) and image a 1.8 km wide and 24 km long box. The white thinner lines on the bathymetric map are other seismic lines acquired during the SISMOSMOOTH cruise. The large white circles indicate the location of ocean-bottom seismometers, and the intersecting white line across axis is the corresponding shot line. The smaller white circles are other ocean-bottom seismometers deployed in a 3-D network during the SISMOSMOOTH cruise. (c) Acoustic backscatter image (located as a white rectangle on the bathymetric map in Figure 1b). Basalts in volcanic seafloor have strong reflectivity, as do scarps in the surrounding ultramafic seafloor. The intersecting ridge axis, emergence, and breakaway of the active detachment fault and the breakaway of one of the inactive faults are indicated as in Figure 1b. A zoom of the 3-D box is shown as a white line, with three black lines indicating the bordering and central lines constituting the box.

2. Geological and Geophysical Setting of Study Area

The easternmost Southwest Indian Ridge between 61°E and 65°E of longitude, and 27°S and 28°S of latitude (Figure 1a), east of the Melville Fracture zone, represents a melt-poor end-member of the global ridge system with nearly amagmatic spreading in corridors of seafloor that extend up to 70 km along-axis (Cannat et al., 2006; Sauter et al., 2013). Large regional ridge depth, high basalt sodium content, positive gravity anomalies, and lower than average seismic crustal thickness have been used to infer an overall low melt supply to the

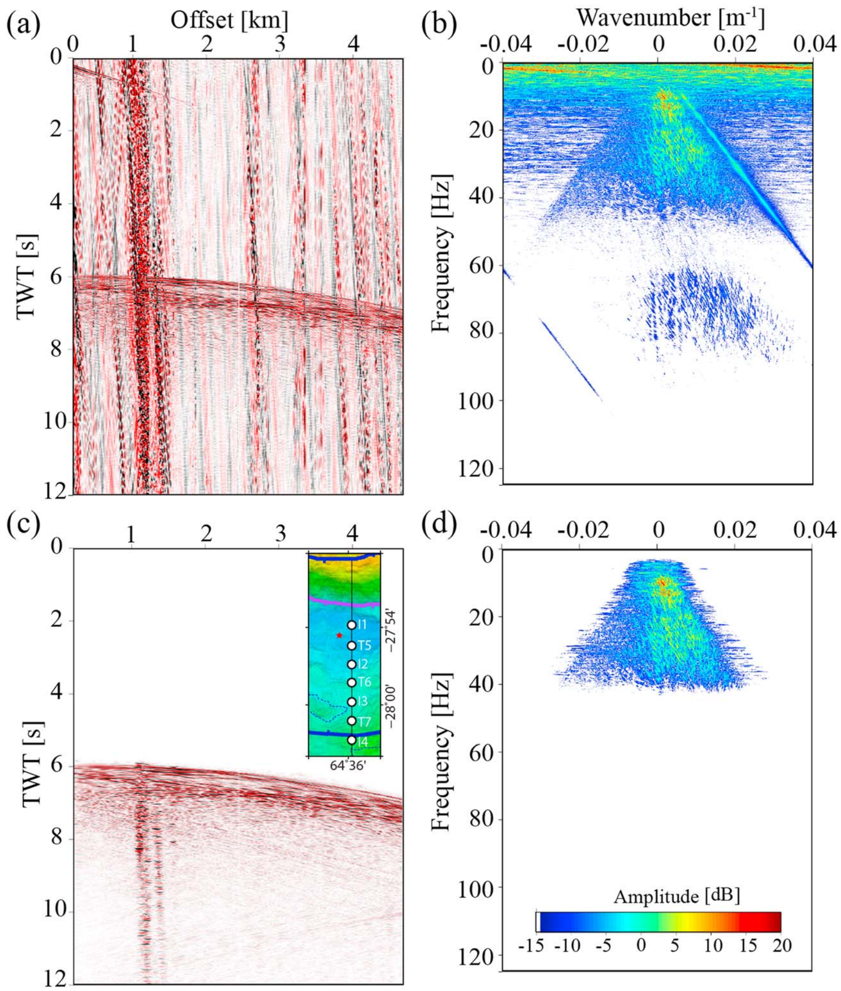

Figure 2. Prestack processing of an example shot gather extracted from the 3-D box. Prior to sorting data to common bin gathers, the shot gathers were muted of direct waves, band-pass filtered with corner frequencies of 6 and 41 Hz and dip filtered. (a) An example raw shot gather. (b) The corresponding amplitude spectra of the raw shot gather in the frequency-wave number (*f-k*) domain. (c) Preprocessed shot gather; the inset shows the location on the bathymetric map from which the shot is extracted (red star). (d) Corresponding amplitude spectra of the preprocessed data in the *f-k* domain.

easternmost SWIR (Cannat et al., 1999, 2006, 2008; Minshull et al., 2006; Muller et al., 1999; Seyler et al., 2003). Within this low melt supply ridge region, there is little evidence of resolvable volcanic cones on bathymetric maps, and dredge hauls reveal that the seafloor is composed of serpentinized peridotite, with almost negligible magmatic rocks (Sauter et al., 2013). Such domains of nearly amagmatic spreading have been called the “smooth seafloor” (Cannat et al., 2006) and are interspersed by more volcanic domains.

Our focus area is centered on the SWIR axial region at 64°35′E of longitude and 28°S of latitude (Figure 1b). The northern wall of the axial valley there forms an ~30 km long (along axis), and up to 2.5 km high massif, that is interpreted as the exhumed footwall of an active detachment fault, postulated to root steeply into the mantle (Sauter et al., 2013). The exposed detachment surface extends from the emergence of the fault to its inferred breakaway (Figure 1b). The area surveyed in our study also extends to the south over the axial domain to the inferred breakaway of a former, north dipping detachment fault (Sauter et al., 2013). Sidescan sonar data over this axial domain (Figure 1c) image rare and localized outcrops of basalts that appear to have erupted directly on the smooth ultramafic seafloor (Sauter et al., 2013).

A previous seismic refraction experiments was carried out at 66°E, just east of our study area. Though confined to more volcanic seafloor, this seismic refraction study has delineated 2.2–5.4 km (~4.2 km on average) crustal thickness, defined by model P wave velocities ≤7 km/s (Minshull et al., 2006), thinner than the classical

6–7 km thick oceanic crust (White et al., 1992). The seismically estimated crustal thicknesses derived from this model were used to benchmark a gravity-based crustal thickness model proposed by Cannat et al. (2006) for the easternmost SWIR region.

A passive seismic experiment carried out at a volcanic center (Segment 8 volcano) located on-axis the SWIR at longitude 65°E to 66°E, east of our study area, reveals local earthquakes down to depths of 25 km below the seafloor, with a trend to deeper earthquakes in less magmatically robust regions of the axis (Schlindwein & Schmid, 2016). Such deep earthquakes suggest that the brittle part of the lithosphere there is at least 25 km thick, and therefore substantially thicker than at the faster-spreading Mid-Atlantic Ridge (Toomey et al., 1988; Wolfe et al., 1995). Schlindwein and Schmid (2016) also show that most earthquakes in the less volcanic regions of the axis occur in a 10 to 15 km thick band and that the upper lithosphere there is aseismic, which they propose due to substantial serpentinization.

Table 1
Data Acquisition Parameters

MCS profiles	
Air gun volume	43.02 L
Shot spacing	50 m
Shot depth	12 m
Recording channels	360
Receiver spacing	12.5 m
Receiver depth	18 m
Minimum shot-receiver offset	177 m
Maximum shot-receiver offset	4,665 m
OBS profiles	
Air gun volume	111.27 L
Shot spacing	150 m
Shot depth	14 m
Recording channels	10, 4C seismometers
OBS spacing	2.5–5 km
Receiver depth	3.9–5.01 km
Minimum shot-receiver offset	9.26 km
Maximum shot-receiver offset	27 km

3. Seismic Data Acquisition

The SISMOSMOOTH 2014 experiment (Leroy et al., 2015) was carried out between September and October 2014 onboard R/V *Marion Dufresne*. It comprised 2,000 km of 43 2-D multichannel seismic (MCS) reflection profiles and 2-D/3-D ocean-bottom seismometers (OBS) network for wide-angle refraction data. Of the seismic reflection profiles, a cluster of 18 MCS lines were shot as a quasi-3-D experiment at a line spacing of 100 m in a 24 km long and 1.8 km wide area across the axial valley and its elevated northern wall (Figure 1b).

The shots for this quasi-3-D experiment used an array of 11 air guns with a combined volume of 43.02 L immersed at depth of 12 m and shooting every 50 m. The data were recorded with a 4.5 km long digital streamer, which had hydrophone groups every 12.5 m, realizing 360 data traces per shot. The streamer was immersed at a depth of 18 m with compasses placed at 300 m interval to record relative angular orientations in real time. The minimum offset (distance between the shot and first active receiver) is 177 m, while the maximum offset is 4,665 m. The nominal common bin coverage (inline fold) for the quasi-3-D experiment is 45. The data were sampled at 2 ms, and record length was 18 s. In the seismic reflection data acquisition reported here, useful data were found in the 6–41 Hz frequency band (Figure 2).

For imaging purposes, it is required that the trace sampling (Δx) is a function of the maximum event dip ($\theta_{\max}$), medium velocity ($v_{\min}$), and data attributes, e.g., maximum frequency for which the structural dip is unaliased in the data ($f_{\max}$). Using an average water velocity of 1,500 m/s, and a maximum frequency of 30 Hz, spatial sampling requirements indicate that an optimum trace spacing of 12.5 m can sample structural dips up to 90° without aliasing in the inline direction, e.g., (Yilmaz, 2001):

$$\Delta x \leq \frac{v_{\min}}{4f_{\max}\sin(\theta_{\max})}.$$

To curtail the undersampling in the crossline direction, trace interpolation is done between the inlines so that the 3-D migration performs optimally.

Wide-angle seismic data were also acquired during the SISMOSMOOTH cruise, with 2-D/3-D OBS networks using an air gun array with combined volume of 111.27 L, shooting every 150 m. For the wide-angle data reported in this study, the OBS were spaced 2.5–5 km and deployed along a profile located 550 m to the east of the 3-D seismic reflection box (Figure 1). The acquisition parameters for the MCS and OBS surveys are summarized in Table 1.

4. Seismic Data Processing

4.1. Seismic Reflection Data Processing

The first step in processing the data was to trace the shape of the streamer using angles (referenced to the geographic north) recorded by 17 compass birds spaced 300 m along the streamer. The angles were

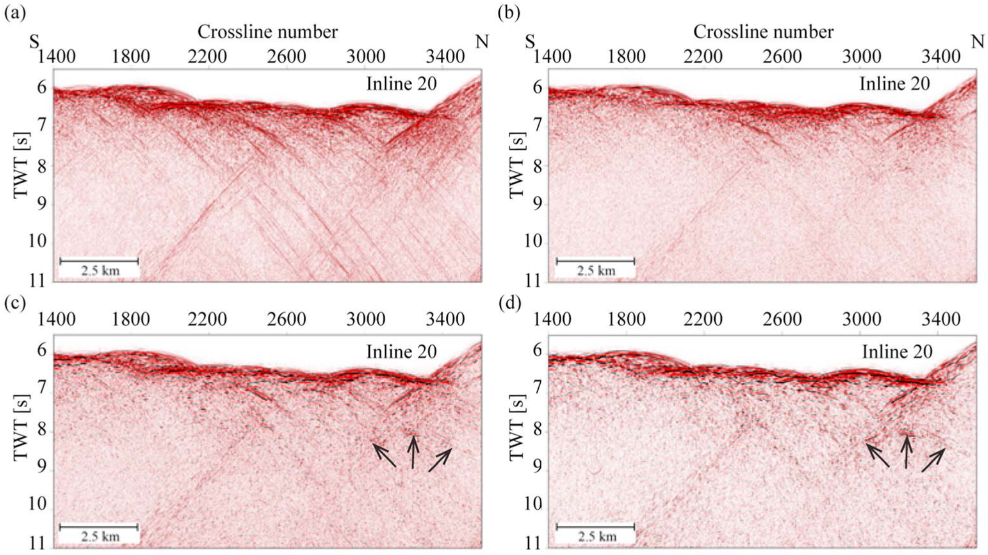

Figure 3. (a) Stack of inline 20 extracted from the central part of the quasi-3-D box (Figure 1b) with normal moveout correction after extended binning. (b) Same stack but including dip-moveout correction with the overall effect of reducing seafloor diffraction tails without revealing the details of the basement. (c) Stack with predictive deconvolution, showing details of the basement, especially a diffraction hyperbola around crossline 3300. (d) Weighted mean filter which eliminated short wavelength noise and revealed the coherency of the diffraction. The arrows in Figures 3c and 3d indicate the diffraction hyperbola.

converted to local distances, which were integrated along the streamer and added to the universal transverse Mercator distances estimated from geographical locations recorded by differential GPS mounted on the vessel.

For the quasi-3-D experiment, the static binning uses 6.25 m in the inline direction and 100 m in the crossline direction; this was elastically extended to 12.5 m inline and 200 m crosslines to harmonize the trace distribution per offset in a given bin. The number of traces in each bin is 45 after dynamic binning. The data were resampled to 4 ms after the application of an antialias filter, so that higher frequencies do not wrap around the data spectrum after resampling. An example of a raw shot gather is shown in Figure 2a, and the corresponding frequency-amplitude spectrum is shown in Figure 2b. What we observe in the shot gather and the *f-k* spectrum is low-frequency noise (0–35 Hz), which spans all wave numbers, a pronounced amplitude decay at the first receiver ghost notch (41 Hz) extending to 60 Hz at normal incidence, and strong amplitude decay from 60 Hz. We have therefore confined the processing to the 6–41 Hz frequency band (Figures 2c and 2d). Preliminary processing at this stage applied a trapezoidal band-pass filter and a dip filter targeted at the subvertical events (low-frequency, long-wavelength swell noise evident in the shot gather in Figure 2a), which may be responsible for the broad noise spectrum in the corresponding *f-k* spectrum, most pronounced between 0 and 6 Hz. The data were binned elastically and sorted to common bin gathers, where the bulk of the processing was implemented. We first tested a range of constant root-mean-square (RMS) velocities for stacking and built a velocity function to stack the data in 3-D. We did not find useful reflections between the seafloor and the first-order multiple for semblance-based moveout velocity analyses, which therefore informed our alternative approach. Comparing stacks produced by this process with those produced from RMS velocities derived from the refraction velocity model, we found both results to be in good agreement. In Figure 3a, we show an example of a stacked section of an inline extracted from the middle of the 3-D box (inline 20), after elastic binning. Dominating this stack are diffractions whose apparent origin is the seafloor. An important processing step to tackle these seafloor diffractions is migration of prestack data to zero-offset (dip-moveout correction) using the log-stretch approach of Liner (1990). This step significantly reduced the seafloor diffractions as shown in Figure 3b. Predictive deconvolution (Robinson, 1967, 1981; Yilmaz, 2001) was applied using a filter designed from an operator length of 400 ms and the third zero-crossing of the autocorrelation of the input trace to reduce the ringiness associated with the source wavelet (Figure 3c). Low-frequency signal enhancement by a weighted mean filter was implemented, and this improved the lateral coherency of the inlines (Figure 3d). In Figure 3d, a diffraction hyperbola is revealed between crossline numbers 3000 and 3400 at 8 s two-way time (TWT).

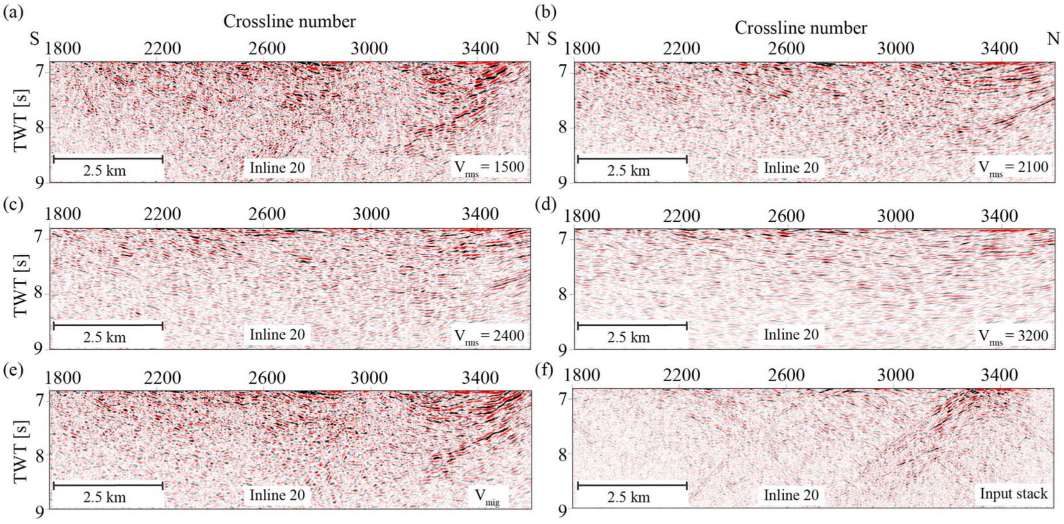

Figure 4. (a) 2-D Kirchhoff poststack migration using constant RMS velocity of 1,500 m/s. (b) 2-D Kirchhoff poststack migration with a constant RMS velocity of 2,100 m/s. (c) 2-D Kirchhoff poststack migrated stack with a constant RMS velocity of 2,400 m/s. (d) 2-D Kirchhoff poststack migration with a constant RMS velocity of 3,200 m/s. Notice below crossline 2600 the degradation of this event with increasing migration velocities. (e) 2-D Kirchhoff poststack migration with a velocity model built from tests of different constant velocity migration. (f) Input stack of inline 20 for the migration tests.

Crossline trace interpolation is critical to increase the spatial sampling in the undersampled crossline direction. This is done by estimating data between inlines. The procedure that we have adopted follows a slant-stack technique where traces are scanned for coherent events in a range of predefined dips between two inlines. For each dip, a semblance is calculated, and the data corresponding to the dips with the highest semblances are stacked and averaged to produce samples for the new (interpolated) trace (Abma & Kabir, 2005; Lu, 1985). This trace interpolation allowed us to increase the spatial sampling from 100 m to 25 m. We increased the width of the 3-D box by padding live traces on the outer inlines to provide sufficient aperture for the 3-D migration operator. This artificially increased the width of the box by a factor of 2. Kirchhoff poststack time migration (Schneider, 1978) was implemented in 3-D to position and focus the amplitudes in space and time. We performed extensive tests of different root-mean-square migration velocities. For flat events, the migration velocity did not impact very much on the result, but for dipping events and diffractions, the velocity is critical (Figure 4). High velocities, which appear geologically (theoretically) admissible, degrade the images, while the extreme case of a low velocity undermigrates the deep events and the limb of a diffractor might appear as a fault. In general, poststack time migration is required to be performed with reduced velocities (e.g., Al-Chalabi, 1994; Etris et al., 2001; Liner, 2004). We build a velocity model for the migration based on tests of different constant migration velocities, which we show in Figure 4. In Figure S2 in the supporting information, we demonstrate the impact of migrating the data using the velocity model derived from tests of constant velocity migrations and with velocity derived from the OBS tomography model.

Although the data acquisition was 2-D (azimuthal coverage = 0) except for streamer feathering, the efficacy of DMO correction and 3-D migration of closely spaced 2-D lines can address some of the challenges such as crossline events appearing on a 2-D line (side swipes) by summing contributions in 3-D volume for a single trace instead of summing contributions from a 2-D area. This comparison is demonstrated in Figure 5, for which the inline shown is extracted from the western boundary of

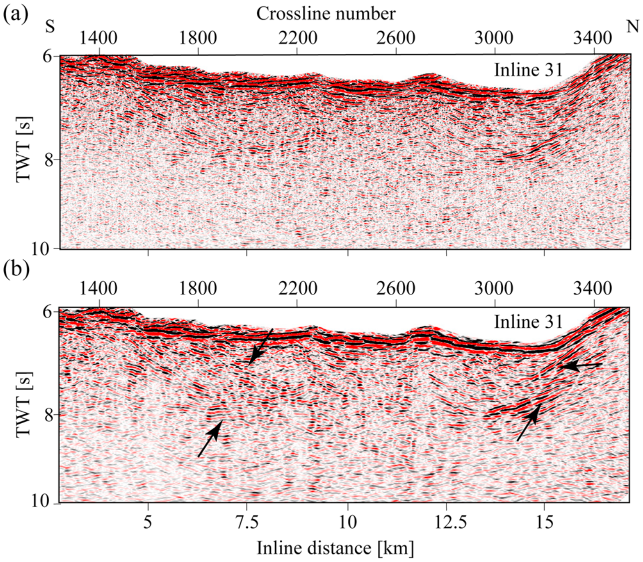

Figure 5. (a) Inline 31 (western end of the quasi-3-D box; Figure 1) after 2-D poststack Kirchhoff migration. (b) Same inline with 3-D migration applied. Note the focusing and coherency of the arrowed events, which show superior quality after 3-D migration compared to 2-D migration.

Table 2
Seismic Reflection Data Processing Steps

Processing Step	Parameters
Data conversion (from SEG-D) to processing environment	
Streamer shape reconstruction and preparation of navigation (.P190) files	
Merge raw data from individual seismic lines with navigation information	
Pre-stack processing	
3D binning	6.25 m × 100 m (static binning); 12.5 m × 200 m (elastic binning)
Resample traces	Resample to 4 ms after antialias filter, 125 Hz cutoff
Mute direct waves	
Ormsby bandpass filter	3-6-41-55 Hz
Coherency filtering	±10 ms/trace
Spherical divergence correction	
Common bin gather sort	45 fold, 6.25 m interval
Velocity analysis 1	
Migration to zero offset	Log-stretch dip-moveout correction
Velocity analysis 2	
Predictive deconvolution	400 ms operator length, third zero-crossing predictive lag (40 ms)
Ormsby bandpass filter	3-6-35-41 Hz
Mean stacking	45 fold
Post-stack	
Weighted mean filtering	11 traces
Crossline trace interpolation	100 m to 25 m
3D Kirchhoff time migration	Root-mean-squared velocity
Post-migration	
Ormsby bandpass filter	3-6-35-41 Hz
Mean filtering	11 traces
Depth conversion	Tomography model velocities.

the quasi-3-D box (inline 31; the location is indicated in Figure 1). The arrows in Figure 5b are used to indicate the areas where we have focused amplitudes of dipping reflectors in a geologically conformable manner, which are not clear in the 2-D migrated result (Figure 5a). In addition, the seafloor appears better imaged after 3-D migration (Figure 5b) than after 2-D migration (Figure 5a). The stronger amplitudes in the 3-D migrated result are attributable to including a volume of traces in the migration aperture in 3-D as against 2-D, which only migrates the data in the acquisition direction. In Kirchhoff imaging, the size of the aperture, i.e., the spatial extent the summation hyperbola spans, is critical for effective migration. It has been suggested that the migration aperture should be at least twice the size of the Fresnel zone (e.g., Sun, 1998; Sun & Bancroft, 2001). Alternatively, the expected horizontal displacement after migration and the common midpoint interval may be used to determine the optimum aperture for migration (Yilmaz, 2001). For the deepest portion of the seafloor in our data, using a zero-offset time of 6.7 s, RMS velocity of 1,500 m/s and dominant frequencies ranging between 8 and 12.5 Hz, the minimum migration aperture required for the seafloor ranges between 1,100 m and 1,400 m. For the deepest part of our zero-offset section where we found useful signals, the required migration aperture for a time of 7.8 s and dominant frequency of 8 Hz is 3,700 m. The aperture requirement for the deep part of our volume is not met due to the narrow width of the 3-D box (1.8 km). Although we performed 3-D migration using the maximum width of the box in the crossline direction, padding the ends of the quasi-3-D box with the inlines on the boundaries to artificially obtain a wider stacked volume did not degrade the results. As shown in the comparison in Figure 5, 3-D migration gives an improved imaging compared to 2-D migration.

It must be emphasized that the imaging in the narrow 3-D box presented in this paper relied on our ability to enhance and migrate low-frequency diffractions (e.g., Bansal & Imhof, 2005; Daley et al., 2002; Davies, 1992; Saenger et al., 2002). Prior to the interpolation, the weighted running average of traces was critical to reduce random noise that masked the diffractions at later times, as the migration fails when these are retained. This procedure smoothes out short wavelength noise and enhances long wavelength signals. Alternative approaches to enhance long wavelength signals are pseudo-V_z deghosting (e.g., Ferber et al., 2013; Momoh et al., 2015, 2016) or sparsity-promoting sparse spike deconvolution. The seismic reflection processing steps are illustrated in Table 2.

4.2. Seismic Refraction Data Processing

We inverted wide-angle traveltimes picked on data recorded by 10 ocean-bottom seismometers (OBS), aligned ~550 m east of the quasi-3-D box (Figure 1b). For our starting model, we built a smooth tomography velocity and sought to iteratively refine this model such that the traveltimes calculated from the refined velocity model match the traveltimes picked on the real data. Our objectives were (1) to estimate the velocity structure in our study area and (2) to use the velocities for depth conversion of the poststack time-migrated seismic reflection images in order to estimate structural dips, and to interpret the reflectivity structure with better confidence.

4.2.1. Data Preparation and Traveltime Picking

Prior to any seismic refraction data processing, the OBS records were relocated using the shots above the instruments and the bathymetry grid. We proceeded by picking the arrival times of the first breaks on unfiltered data and included picks on the noisy parts of the data after applying a minimum phase trapezoidal band-pass filter with corner frequencies 3 and 18 Hz. An example of OBS gather is shown in Figure 6. For plotting the data shown in Figure 6, we used an automatic gain control (7 s sliding window length), an offset-

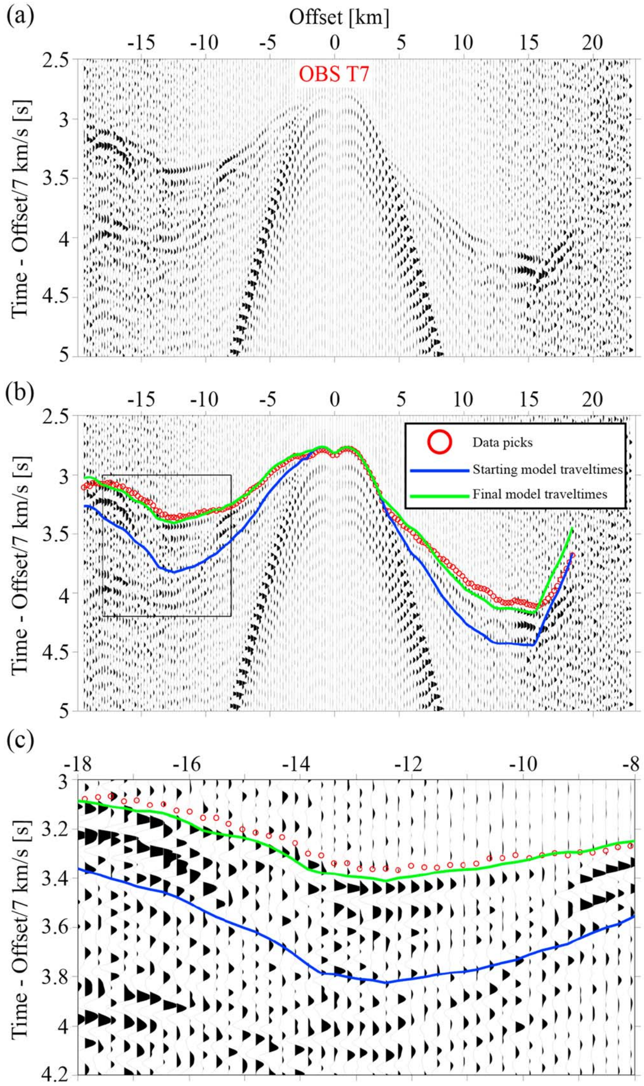

Figure 6. Ocean bottom seismometer (OBS) gather for relocated instrument T7. (a) OBS gather after the application of a trapezoidal filter (1-3-18-25 Hz), offset-weighted gain correction, and automatic gain control (only for display). (b) Same gather as Figure 6a showing the traveltime picks (red circles), synthetic traveltimes computed on the starting model (blue line), and synthetic traveltimes computed for the final model (green line). Note that the traveltime picks on the data were made on raw, ungained data and included picks in the noisy part of the data after applying the trapezoidal filter only. (c) Zoom of the data highlighted by the black rectangular box in Figure 6b, showing the picked traveltimes, calculated traveltimes, and waveforms.

weighted amplitude gain to enhance the data, and a reduced timescale using a reduction velocity of 7 km/s. Picking uncertainties were allocated following an offset-dependent relationship for source-receiver distances less than 15 km. The uncertainties were set as 30 ms at offset = 0 and 80 ms at offsets of at least 15 km. First break arrival times (1608) were picked, with an average uncertainty of 61 ms.

4.2.2. First Arrival Traveltime Tomography

We used the Tomo2D code (Korenaga et al., 2000). The geometry extracted from the picked traveltimes is used to trace the seismic rays in the input model, and traveltime residuals are reduced through an iterative inversion scheme. Our starting model (Figure 7a) starts with a *P* wave velocity of 3 km/s at the seafloor, increasing to 8 km/s 5 km below the seafloor. At greater depths, velocities in the starting model increase with a gentler gradient (0.043 km s^{-1} km). Our preferred final model (Figure 7b) was obtained after six iterations, reducing the χ^2 from 15.13 to 0.96 (χ^2 = 1 would mean that the model fully reproduces the traveltime picks), and t_{RMS} reduces from 263 ms to 63 ms. Figure 8 compares histograms of traveltime residuals obtained with the initial and final model. The residuals after the inversion are clustered around ±0.05 s, compared to the initial residuals which are more widespread (±0.5 s).

4.2.3. Model Resolution

The derivative weight sum (DWS) can be seen as an indication of the ray density in the model (Thurber, 1983) and allows a first estimation of the areas of the model that are optimally resolved. Figure 9a shows that this is the case at model distances 7 to 34 km and depths 3–8 km, with large DWS values, and rays travelling in both directions.

A qualitative model resolution is obtained using checkerboard tests. We introduced ±5% sinusoidal velocity anomaly patterns in the final model, computed traveltimes in this perturbed model, and added random Gaussian noise to these calculated traveltimes, assuming two components to the traveltime error: (1) the common receiver error up to ±50 ms for each receiver (Zhang & Toksöz, 1998) and (2) traveltime picking errors up to ±30 ms or ±80 ms (i.e., the uncertainty depending on the offset) for each pick. We inverted the perturbed/randomized picks and compared the result with the final model of Figure 7b to plot the recovered anomalies. Checkerboard structures of 4 × 1 km (Figure 9b) and 4 × 2 km (Figure 9c) are well recovered in the central and upper part of the model (8–30 km model distance and depths <8 km), where the ray coverage is densest (Figure 9a).

In order to further assess model resolution, we also used a Monte Carlo analysis. We generated (1) 100 independent randomizations to the picked traveltimes following the same strategy used for the checkerboard tests and (2) 100 input models, randomized from the starting model presented in Figure 7a. Input models were built with *P* wave velocities of 3 ± 0.15 km/s at the seafloor, 8 ± 0.3 km/s at 5 ± 1 km below the seafloor, and a velocity gradient below 0.005–0.065 km s^{-1} km. The standard deviation (σ) is shown in Figure 9d. The χ^2 values in the final models range from 0.88 to 1.11, with an average value of 0.98. We observe that σ are <50 m/s in the central and upper parts of the model, in the area where ray density is highest (Figure 9d), and checkerboard patterns are reasonably well recovered (Figures 9b and 9c). The σ increases rapidly to at least 150 m/s on the flanks and base of the model (Figure 9d), where ray density is low or travelled in one direction (Figure 9a). The average of the 100 Monte Carlo models after six iterations (Figure S4 in the supporting information) is nearly identical to the final *P* wave velocity model shown in Figure 7b.

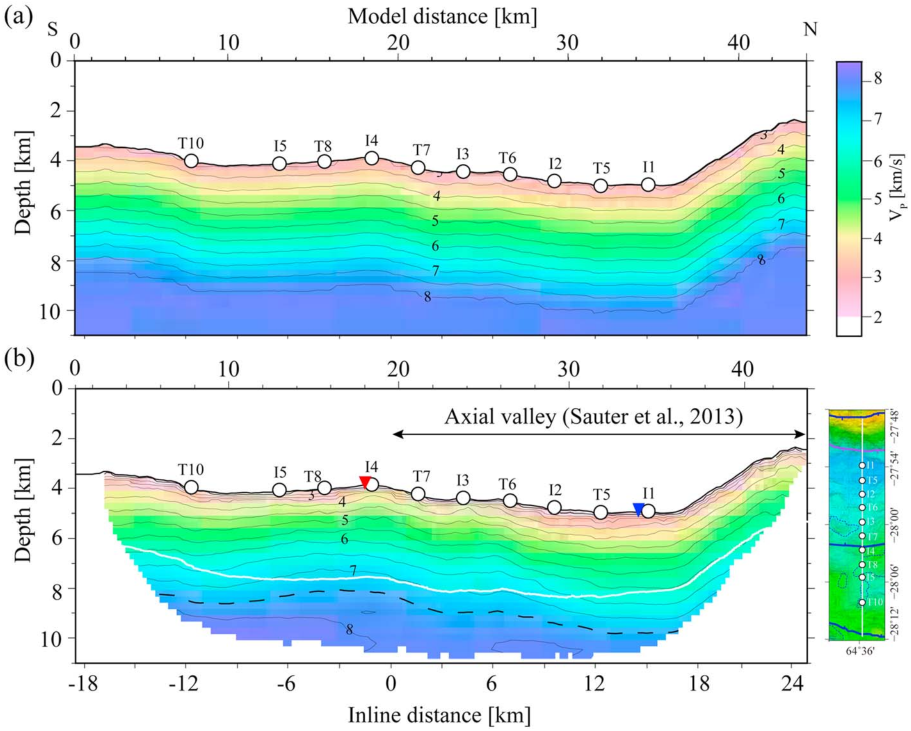

Figure 7. (a) Starting *P* wave velocity model for the tomography inversion. The rounded circles are the OBSs annotated in Figure 1. (b) Final velocity model obtained after six iterations. The base of the crust derived from constant density gravity modeling is plotted as a white line (Cannat et al., 2006). This gravity-derived model was benchmarked to seismically defined crustal thicknesses in the east of our study area (Minshull et al., 2006), using 7 km/s iso-velocity contours for the base of the crust. The 7.5 km/s iso-velocity contour (black dashed line) would correspond to peridotite with ~16% serpentinization (Miller & Christensen, 1997). The inverted triangles show locations of 1-D velocity profiles shown in Figure 12. Locations of the OBS line are shown in the sections (circles) and on the bathymetric map extract, to the right of Figure 7b.

5. Results

5.1. 3-D Seismic Reflection Volume

The output of the 3-D Kirchhoff poststack time migration in our study area is a seismic volume, 19 km in length and 1.8 km wide, built from processing the eighteen 100 m spaced MCS profiles (Figure 10). Our interpretation strategy was to identify reflection events in the middle profiles where we expect optimum migration, then pick these events successively in the eastern and western profiles wherever they can be followed coherently. Figure 10b only shows a selection of those reflectors that could be picked in at least three adjacent profiles (i.e., 360 m). These laterally continuous reflectors belong to four distinct families, according to their dip, dip direction, and depth range: north dipping reflectors in the axial domain, south dipping reflectors beneath the elevated northern wall of the axial domain, and two sets of flat-lying reflectors in the shallow and deep TWT range. In this section, we examine the characteristics of the reflectors in each family, i.e., dip and depth, where depth conversion is done with velocities extracted from the *P* wave tomography velocity model (Figure 7b). We computed the thickness in each time interval using the *P* wave velocity within the interval and integrated the interval thicknesses to retrieve the depths. This is identical to a vertical stretch of the seismic traces.

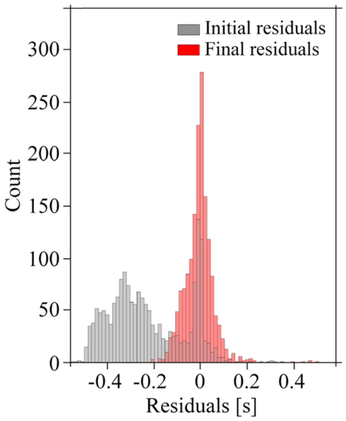

Figure 8. Histrograms of traveltime residuals for the initial (grey) and final (red) velocity models. Bin size is 15 ms.

5.1.1. South Dipping Reflectors

The most prevalent events imaged in our 3-D volume are south dipping reflectors identified in the northern part of the 3-D box, below

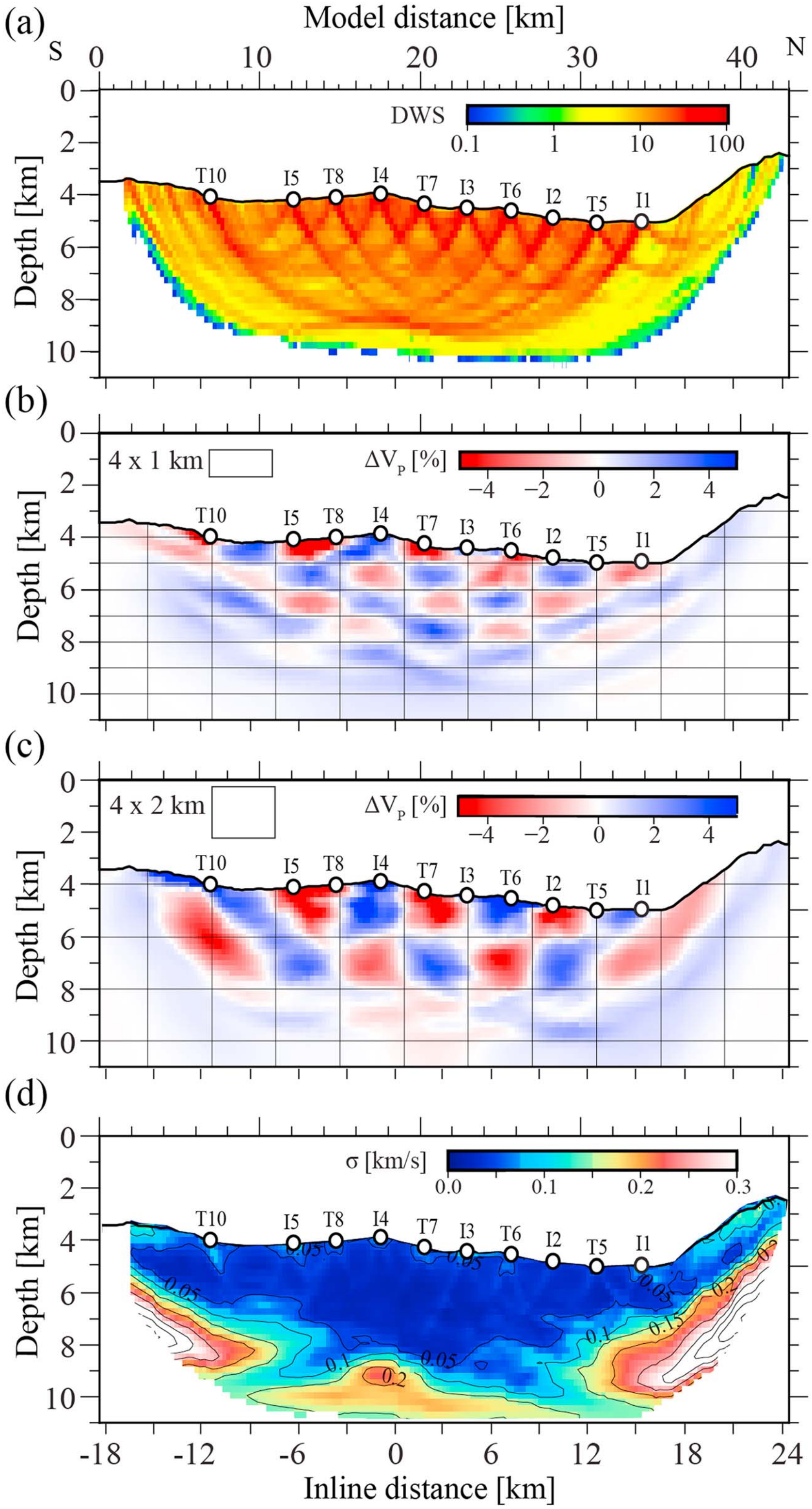

Figure 9. Model resolution tests. (a) Derivative weighted sum (a measure of ray density) showing the ray coverage for the *P* wave velocity model shown in Figure 7b. Ray coverage is optimum in domains colored in yellow and red. (b) Checkerboard tests designed to assess the qualitative resolution for the velocity model shown in Figure 7b. Sinusoidal velocity perturbations introduced using 4 × 1 km grid structures. (c) Checkerboard test using 4 × 2 km grid structures. Structural resolution is optimum where the ray density is optimum. (d) Standard deviation calculated from the Monte Carlo analysis (see text).

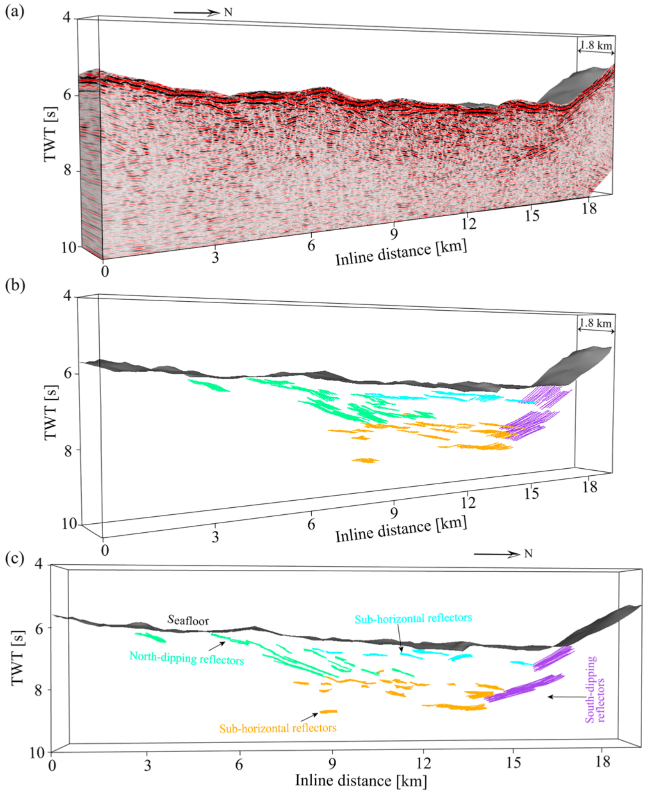

Figure 10. (a) Perspective view of the 3-D processed seismic volume with inline 13 on the forefront. The displayed box is 19 km long and 1.8 km wide (Figure 1). It is viewed from the SSE. (b) 3-D perspective view of the line drawings of the interpreted events (reflectors) picked in each of the 19 inlines of the 3-D time-migrated seismic volume, and viewed from the same direction as Figure 11a. (c) Same as Figure 10b but viewed from the east. Four distinct categories of events are observed: south dipping events (in purple), north dipping events (in green), and two categories of subhorizontal reflectors occurring in the shallow TWT (cyan) and deep TWT (orange) regions of the processed volume. Seafloor topography is derived from picking the seafloor reflectivity from poststack time-migrated volume, and interpolating data between the picks.

the emergence of the active axial detachment fault (Figure 1b). They extend across-axis over the full 1.8 km width of the 3-D box (Figure 10b). They occur in two distinct packages that are horizontally and vertically offset, with the horizontal offset decreasing toward the eastern part of the 3-D box. The depth-converted image for inline 31 (Figure 11; results for inlines 13 and 22 are shown in Figure S3 in the supporting information) indicates that the south dipping reflectors are steep (~45–60°). Beneath each of these main reflectors, we observe packages of weaker and less laterally continuous subparallel reflectors that extend vertically over ~0.5 s TWT (Figure 11a). The horizontal separation between the two main south dipping reflectors ranges between 0.16 km (in the eastern part of the 3-D box) and 0.68 km (in the western part). Their vertical offset ranges between 0.8 and 1.4 km. The upper south dipping reflector can be followed to depths of ~2 km below the seafloor (Figures 11b and S3 in the supporting information). The lower south dipping reflector can be traced to depths of ~5 km below the seafloor. We show the stacks, and corresponding common bin supergathers of selected inlines to highlight the events interpreted as the south dipping reflectors in Figure S1 in the supporting information.

5.1.2. North Dipping Reflectors

The north dipping reflectors are observed in the southern part of the axial domain surveyed in this experiment. The reflectors are interpreted in the central part of the 3-D box, below the axial valley and over the entire 1.8 km width of the 3-D box (Figure 10b). They occur as a series of closely spaced reflectors (1–2 km) over an across-axis distance of ~9 km (inline distances between ~2.7 and 12 km) and between 6 and 7.5 s TWT in the 3-D time-migrated volume (Figure 10b). In Figure 11a, they are shown between inline distances 5 and 10 km (down to 1.5 s TWT below the seafloor). In the depth-converted image shown in Figure 11b, they can be traced to depths of ~4 km below the seafloor. In the deeper part of the section where they are imaged, they dip 35–45°. In the shallowest part (<1.5 s TWT), some of the north dipping reflectors are shallow-dipping (30°). Though there is no clear evidence in our seismic image that these reflectors offset the seafloor, a few, if projected with the same dip onto the seafloor, conform to scarps <200 m high at inline distances 4.8 to 8 km. These scarps are interpreted as minor faults (Sauter et al., 2013). Another shallow reflector is imaged very near the seafloor at 2.7–2.8 km inline distance below basalt outcrops (indicated at 64°36′E longitude and 28°S latitude) shown in Figures 1b and S5 in the supporting information.

5.1.3. Subhorizontal Reflectors

The third and fourth classes of reflectors are deep and shallow subhorizontal reflectors. The subhorizontal reflectors in the deep part occur at 7.5–9 s TWT between inline distances 8 and 14 km of the time-migrated 3-D volume (Figure 10b). They are mostly visible in the central and the western parts of the 3-D box (inline 31 shown in Figure 11a). They occur in the proximity of the deepest portion of the north dipping reflectors (~4 km below the seafloor) as shown in Figure 11b. They can also be observed ~5 km below the seafloor, adjacent to the deepest portion of the south dipping reflector (Figure 11b). An inline with a corresponding common bin supergather is shown in Figure S1c to highlight one of the subhorizontal reflectors prominent in the prestack gathers.

The shallow subhorizontal reflectors are identified <1 s TWT below the seafloor and between inline distances 8 and 16 km (Figure 10b). In Figure 11b, they occur just below the seafloor reflector (<1 km). Toward the central part of the 3-D box, the shallow subhorizontal reflectors are ubiquitous between the south dipping reflector and the north dipping reflectors, while toward the east, they are observed mostly below the seafloor at

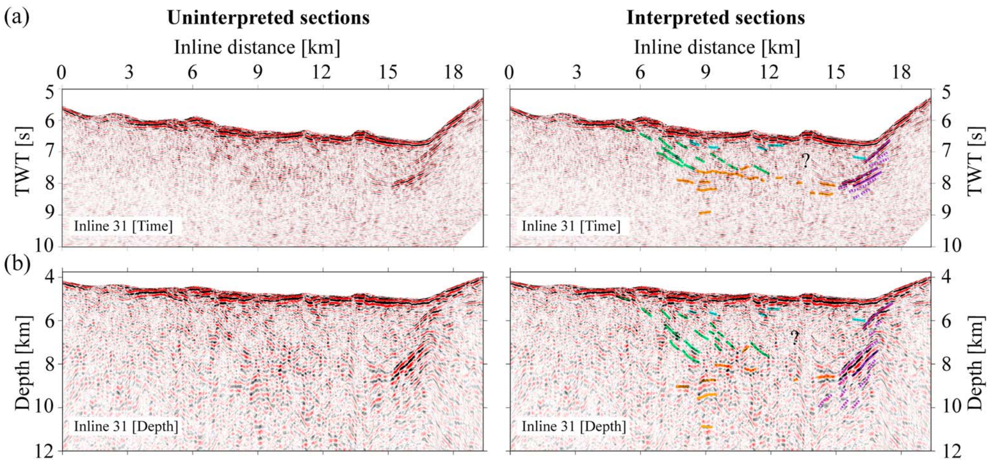

Figure 11. Time-migrated and depth-converted sections of inline 31. (a) Cross section in time of inline 31 (west of the 3-D box). (b) Cross section in depth of inline 31. The depth conversion is done with velocities extracted from the *P* wave velocity model (Figure 7b). The time section is shown with the interpretation of inline 31 from the 3-D volume (see Figure 10), and the corresponding events in the depth domain. Vertical exaggeration of depth section = 1.

the 12 km inline distance, below the deepest part of the seafloor. In general, the shallow subhorizontal reflectors are observed to depths of <1 km below the seafloor, as disjointed, but coherent events throughout the width of the survey area.

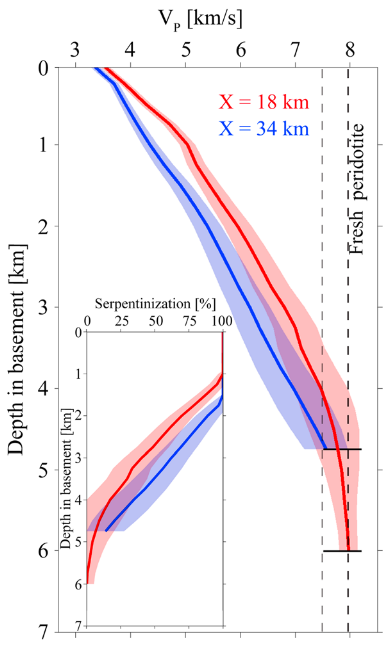

Figure 12. 1-D velocity profiles extracted from the final *P* wave velocity model at model distances (*X*) = 18 km and *X* = 34 km (locations are indicated in Figure 7b). Each profile is shown with the standard deviation derived from the Monte Carlo analysis. The dashed lines correspond to 7.5 km/s and 8 km/s *P* wave velocities. The inset shows the corresponding fraction of serpentinization computed from the empirical relationship between compressional wave velocity and serpentinization proposed by Miller and Christensen (1997). The plots are truncated where the ray coverage is very low, which are shown here as horizontal black lines (Figure 9a).

5.2. Compressional Wave Velocity Model From Traveltime Inversion

The 2-D *P* wave velocity model in Figure 7b is a smooth model where crustal-type velocities (which we chose to define as *P* wave velocities <7.5 km/s) prevail in the upper 4 to 5 km. We chose this 7.5 km/s *P* wave velocity value because it is the maximum velocity measured for olivine-rich gabbros (Miller & Christensen, 1997). Any rock type with *P* wave velocities higher than that would therefore qualify as an ultramafic rock. The 7.5 km/s iso-velocity contour could correspond to peridotite with ~16% serpentinization (Miller & Christensen, 1997). This seismically defined crustal layer is thicker than the gravity model-defined crustal layer of Cannat et al. (2006). It should be noted, however, that this gravity-derived model was benchmarked to seismically defined crustal thicknesses in the east of our study area, using 7 km/s iso-velocity contours for the base of the crust (Minshull et al., 2006). Two 1-D velocity-depth profiles, extracted at 18 and 34 km model distances (Figure 12), show a nearly linear increase of velocity with depth from the seafloor (at 34 km), or below 1 km (at 18 km). Velocities are 0.5 km/s to 1 km/s lower at any given depth in the profile extracted at 34 km model distance (Figure 12), near the emergence of the active south dipping detachment fault (Figure 1b).

Figure 12 also shows the estimated volume percentage of serpentinization that could correspond to model *P* wave velocities, computed from an empirical relationship between *P* wave velocity and serpentinization (Miller & Christensen, 1997). This provides an estimate percentage of serpentinization in the end-member case for which the crustal velocity structure is fully produced by variable serpentinization of the exhumed mantle peridotite. In this end-member case, serpentinization would be 100% in the upper 1 km (at 18 km model distance), or 1.6 km (at 34 km model distance), then decrease to 16% at the base of the

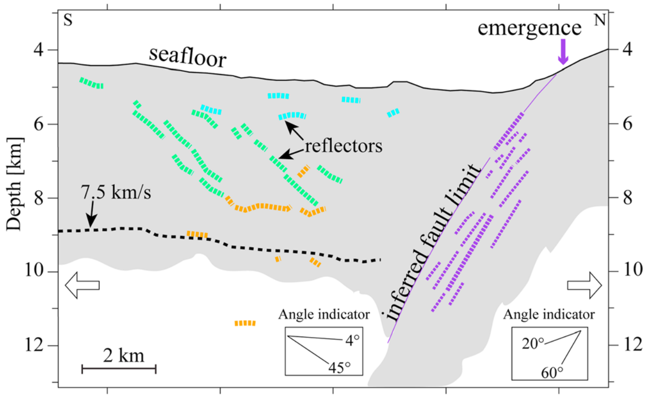

Figure 13. Sketch integrating the results from the 3-D seismic reflection volume and wide-angle *P* wave velocity model. The dashed thick purple markers trace the bright amplitude reflectors in the footwall of the axial detachment fault. The thinner dashed purple lines indicate areas where weak amplitude reflectors are persistent with similar southern dips. The principal fault plane (i.e., the limit between the hanging wall and footwall plate) is inferred and shown as a continuous purple line. The green dashed lines are the north dipping reflectors imaged in the axial valley domain (hanging wall of the active detachment fault). The base of the crust, which we propose as corresponding to the transition from serpentinized peridotite to fresh mantle, is sketched on the 7.5 km/s velocity contour. This contour is represented only in the domain where it is well resolved by the OBS data (Figure 9a). The serpentinized crustal layer (pale grey) is inferred elsewhere (see text). The orange dashed lines represent the subhorizontal to slightly dipping reflectors that are imaged within 1–2.5 km proximity from the base of the crust, and in the mantle. The seismic imaging capabilities of our acquisition setup are limited to depths of ~11 km below the sea surface (~6 km below the seafloor). The interpretation of this sketch is discussed in the text.

seismically defined crust (here proposed to correspond to the 7.5 km/s velocity contour).

6. Interpretation and Discussion

The quasi-3-D seismic reflection and wide-angle seismic refraction data analyzed in this study provide constraints to test hypotheses proposed for the formation of the oceanic crust at very low melt supply and ultraslow spreading rate.

Despite the very low melt supply, our results show that the low seismic velocity crustal layer (*P* wave velocity 3.5–7.5 km/s) is 4 to 5 km thick. This seismically defined crustal layer contains several categories of seismic reflectors. In Figure 13, we show a geological sketch based on the integration of the depth-converted 3-D seismic volume and the *P* wave velocity structure in our study area. We have outlined the most persistent reflectors in the 3-D volume (as shown in Figure 10b), and now examine how they may have formed, and their implications for crustal evolution in our study area.

We will first examine the south dipping reflectors and interpret them as corresponding to the damage zone of the active axial detachment fault. We will discuss how this damage zone develops and how it could aid in the serpentinization process in the footwall. We then examine the seismic structure of the basement in the hanging wall of the active axial detachment fault, below the axial valley seafloor. The predicted fate of this seafloor domain is not to be passively transported off-axis as part of the Antarctic plate. We therefore view this domain as representative of the "end-product" of melt accretion, just before it leaves the axial region. Finally, we compare our *P* wave velocity model with models from other magma-poor plate divergence domains, i.e., mid-ocean ridge environments where mantle rocks have been exhumed and domains of documented or inferred ultramafic basement at ocean-continent transition zones.

6.1. Detachment Faulting and Serpentinization

The south dipping reflectors occur beneath the proposed emergence of the active axial detachment fault (16–19 km inline distance in Figure 10). They occur as two bright and laterally continuous reflectors, offset in depth and horizontally as outlined in Figure 10, and several less bright and less laterally continuous subparallel reflectors. In the interpretive sketch of Figure 13, we propose that the outer bound of the damage zone, which is the limit between the footwall (African plate) and the hanging wall (Antarctic plate) domains, corresponds to the downward continuation of the upper south dipping reflector. We propose that it steepens at depth to parallel the deeper bright reflector (50–60°). This deeper reflector is offset horizontally by 1.6 km into this proposed footwall domain. Weaker amplitude events, which are focused in the proximity of the bright amplitude reflectors—interpreted on the time-migrated volume (Figures 10b and 10c), can be observed in Figure 11b, between 15 and 18 km inline distances.

The fault zone as inferred from seismic constraints dips at least 45° up to 2 km of its emergence at the seafloor. The seafloor in the footwall compartment, however, dips only 20° on average (Figure 13). Recently acquired high-resolution bathymetry data and submersible observations (Cannat et al., 2017) indicate that this difference is best explained by extensive mass-wasting of the exposed part of the footwall when the fault dip at emergence is more than the stability angle, as proposed for axial detachment faults at the Mid-Atlantic Ridge (Cannat et al., 2013).

The maximum horizontal distance between the proposed hanging wall/footwall boundary and the weaker south dipping reflectors (Figure 13) is 2–2.8 km. We interpret this reflective domain as the damage zone of the fault. This seismically defined domain could either be a finite damage zone, created over time due to

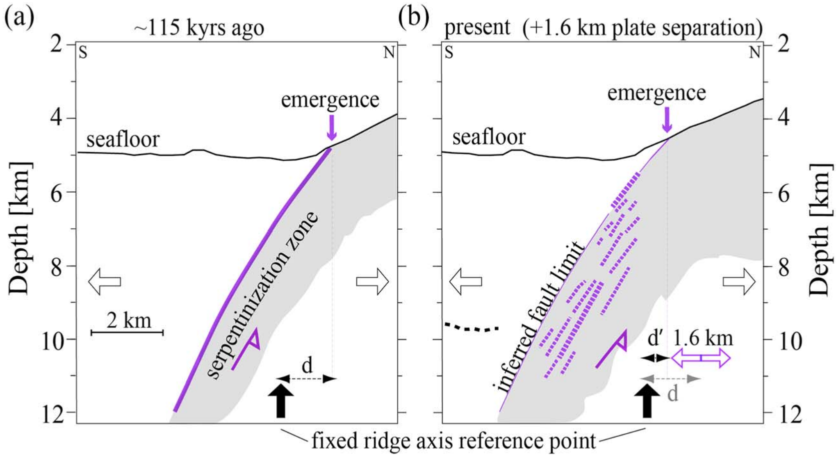

Figure 14. Conceptual sketch of the evolution of the axial detachment fault damage zone in our study area. (a) At an early stage some 115 kyr ago. (b) At present, with seismic reflectors represented as in Figure 13. The principal fault plane (i.e., the limit between the footwall and hanging wall plates) is inferred and shown as a continuous purple line in Figures 14a and 14b. The pale-grey shading in the footwall corresponds to the inferred finite damage zone, which is inferred to be preferentially serpentinized. In the sketch, we propose that this domain of serpentinized and fractured peridotite thickens as fault displacement increases. At *M* (magmatic contribution to plate divergence) nearly zero, the fault is predicted (Buck et al., 2005) to be moving away from the ridge axis (black arrow) at a maximum velocity equal to half-spreading rate. The ridge axis is where mantle material is supplied from the lower ductile lithosphere, to the fault's footwall. We propose that moving the fault away from this supplying region should promote internal deformation of the footwall. While the frequency of the fractures defining the damage zone at any given time decreases with distance from the fault core (Gudmundsson et al., 2010, 2013), we thus propose that fault displacement becomes partitioned over a wider finite damage region as fault displacement increases. This is schematically represented here with 1.6 km additional plate divergence (or 115 kyr) between Figures 14a and 14b. The distance between the fault emergence and the axial reference point decreases by 0.8 km (half of the plate divergence) between Figures 14a and 14b, and finite width of the damage zone increases by a similar amount.

strain localization in a succession of subparallel fault segments within the footwall, or an instantaneous damage zone due to distribution of active deformation over a thick domain of subparallel fractures, or a combination of both. The abundance of the fractures defining a fault's damage zone at any given time decreases with distance from the fault core (Gudmundsson et al., 2010; Gudmundsson et al., 2013). A broad zone of distributed instantaneous deformation could form if the rheology of the footwall rocks is such that strain localization is not efficient. This could be favored both by the scarcity of the weak mineral talc in the fault rocks dredged in the area (Cannat et al., 2012) and by the thick brittle axial lithosphere inferred from the depth of microearthquakes ($>$20 km; Schlindwein & Schmid, 2016).

A broadening of the finite damage zone with time as fault displacement increases is also a possibility. In the melt-starved context ($M \approx 0$) of plate divergence that corresponds to our study area, it is predicted (Buck et al., 2005) that the fault should migrate with the hanging wall plate to accommodate the far-field pull of plate divergence, which in the presence of magma ($M > 0$) would be taken by dyke intrusions. As a result of this migration, the fault probably moves toward the south with respect to the ridge axis at a rate close to the half-spreading rate of 7 mm/yr. The ridge axis is where mantle material is being supplied from the lower ductile lithosphere to the fault's footwall. We propose that moving the fault away from this supplying region could promote internal deformation further into the footwall. A two-step conceptual sketch of this scenario is shown in Figure 14.

In step 1, the fault at a prior stage is represented by a principal fault plane with fracturation-induced serpentinization in the footwall (e.g., Cannat et al., 2010). In step 2, the accretionary deficit in the hanging wall induced by the far-field pull of plate tectonics and the long-lived melt starvation causes the fault limit to extend toward the hanging wall while the fault damage zone expands into the footwall.

The development of a 2–2.8 km thick fault damage zone, whether finite or instantaneous, provides a mechanism by which serpentinization could reach deep into the ultramafic basement. Faults and the associated fracture networks would serve as pathway for seawater to ingress into the footwall, hydrating the exhumed peridotite (Rouméjon et al., 2015). Indeed, the most fractured parts of the footwall could also be the most serpentinized, creating the impedance contrast that produces the south dipping reflective packages imaged in this study. Oxygen isotope data on samples dredged in our study area (Rouméjon et al., 2015) indicate that the bulk serpentinization occurred in the most kinetically favorable temperature window for serpentinization (~250–350°C). If the cold thermal context inferred from microseismic studies (Schlindwein & Schmid, 2016) is correct, such temperatures would likely be reached deep in the fault, probably deeper than the limit of the seismic reflection and refraction data presented in this paper. Such high temperatures of serpentinization are also a strong argument against the more classical serpentinization front model, whereby serpentinization proceeds from the seafloor downward due to thermal cracking (Lister, 1974).

Resolution tests (Figure 9) show that the *P* wave velocity model of Figure 7b does not resolve the velocity structure in the axial detachment fault's footwall. It does, however, indicate that *P* wave velocities in the hanging wall near the fault (34–38 km in the velocity model of Figure 7b) are 0.5 km/s to 1 km/s lower at any given depth than further away from the fault (Figure 12). We propose that this is due to enhanced fracturation and possibly also enhanced serpentinization of the ultramafic basement in the hanging wall (Antarctic) plate near the active detachment fault.

6.2. Internal Structure of (Geophysically Defined) Oceanic Crust Formed at Nearly Zero Melt Supply

The seismic experiment we report on was designed to provide the best resolved constraints on the seismic reflection and velocity structure at the ridge axis, in the hanging wall of the presently active axial detachment fault (Figures 1 and 13). Dredging and imaging of the seafloor indicate that this axial domain has a flat ultramafic basement with occasional hills made of few hundred meters of basalt that have erupted onto the ultramafic seafloor (Cannat et al., 2006; Sauter et al., 2013; Figures 1b and 1c). This ultramafic seafloor is proposed to have formed in the footwall of a previously active north dipping axial detachment fault (Sauter et al., 2013). It is now being passively transported to the south, as part of the Antarctic plate, and can therefore be viewed as representative of the end-product of melt-starved accretion, just before it leaves the axial region. Reflective events in this axial domain could have originated as part of the earlier, footwall-located history of detachment faulting or due to more recent minor faulting and sparse volcanism at the ridge axis.

Seismic velocities in this axial domain are between 3.5 and 7.3 km/s in the first 4–5 km below the seafloor (Figure 7b). At $<$1.5 km below the seafloor (8–16 km inline distance), we imaged discontinuous subhorizontal reflectors (Figure 11). They occur where the *P* wave velocity is $<$5 km/s (28–36 km model distance as shown in Figure 7b), therefore lower than *P* wave velocity for full serpentinization (Miller & Christensen, 1997). These observations can be explained by pervasive fracturing in the upper 1.5 km in the axial domain, which enhances the porosities locally (e.g., Detrick et al., 1994; Spudich & Orcutt, 1980). We further explain the reduced velocities as being due to fluid incursion in these fractures. Even though the velocity range in the upper 1.5 km in the basement overlaps that for fractured basalts, the typical high-velocity gradient associated with layer 2A/2B transition is not replicated in our study area.

A persistent set of reflectors in the axial domain is the cluster of north dipping reflectors imaged between 2.7 and 12 km inline distance (Figures 10b, 10c, and 11). These reflectors occur where the *P* wave velocity ranges between 3.5 km/s to 6.5 km/s. At 4.8 and 8 km inline distances, these reflectors can be projected up to very near the seafloor (Figures 10c, 11, and S5 in the supporting information) and some appear to correspond with small normal offsets ($<$200 m). One of the faint north dipping reflectors locally visible at shallow depths on the 3-D migrated volume (i.e., 2.7 km inline distance) underlies an isolated basaltic patch (Figures 1 and 11). Based on these observations, we consider three possibilities for the origin of the north dipping reflectors.

In the first two hypotheses, the north dipping reflectors are relatively recent features, formed due to the axial valley tectonics and/or volcanism. First, they could be dykes feeding melt to areas where sparse volcanism is observed on the seafloor. This would explain their locally strong reflective characteristics. Second, they may correspond to antithetic conjugate minor faults formed in the hanging wall of the axial detachment fault to accommodate the tectonic pull on the Antarctic plate. Numerous minor offsets of the topography (Sauter et al., 2013) and significantly reduced velocities in the upper 2 km compared to other parts of the model (5–15 km inline distances) as shown in Figure 7b are indeed consistent with active tectonic stretching in the axial valley. However, observed offsets of the axial valley topography face both north and south and do not indicate a strong prevalence of north facing faults, while only a few north dipping reflectors do

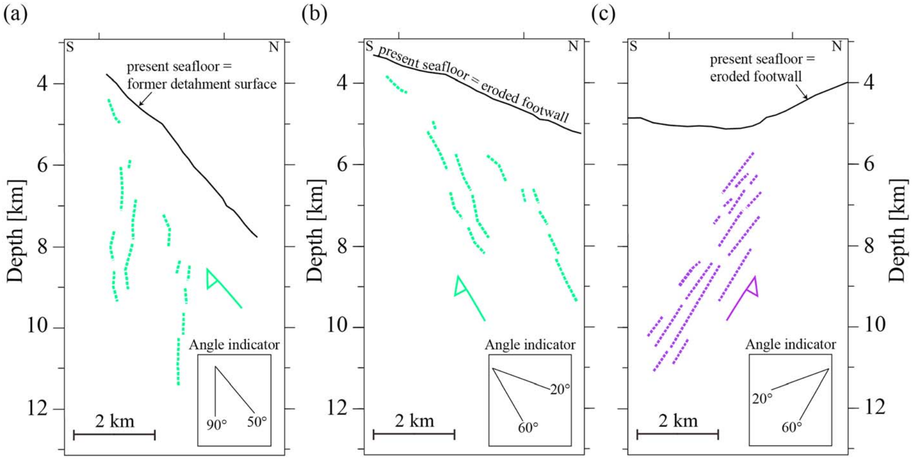

Figure 15. Conceptual models and comparison with present-day detachment fault geometry to discuss the "inheritance" hypothesis for the origin of the north dipping reflectors detected in the hanging wall of the active south dipping axial detachment fault. In the two cases, the reflectors are inferred to have formed in the footwall of a previous north facing detachment fault. (a) Case 1: assuming footwall roll-back of 45° without significant erosion, the events were vertical at depth for a fault active at 45–50°. (b) Case 2: assuming the exposed footwall was significantly eroded and the exposed surface dips similar to the present-day exposed footwall (20°), back-rotating the previous footwall by an angle of 15–20° indicates that their dips are analogous to the present-day configuration, but the lateral offsets are larger. (c) Present-day configuration of the damage zone of the detachment fault. Although we cannot unambiguously discriminate the exact origin of the north dipping reflectors, comparing them with the present-day detachment fault geometry allows us to propose as one possibility that they may be inherited from a previous episode of north facing detachment faulting, which included a rollback to rotate them to their current dips.

project to seafloor offsets. Therefore, if the second hypothesis is correct, the reflectors would correspond to small offset faults or fractures that do not for the most part reach the seafloor. It is not clear why they should be so reflective in this case, unless these small offset faults or fractures also serve as melt conduits (combination of hypotheses 1 and 2).

Our third hypothesis is that the north dipping reflectors may be interpreted in the context of the flip-flop hypothesis (Sauter et al., 2013) as inheritance from internal deformation in the footwall of the previous north facing detachment fault. Two scenarios can be considered for this inheritance hypothesis. In the first scenario, we assume that the seafloor in the axial domain, which presently has a very low southward slope (4° on average), represents the exhumed surface of this former north facing detachment fault. In this case, and assuming a 50° northward dip for this detachment fault (Figure 15a), undoing the flexural rollback to 4° (i.e., 46° rollback) would bring the reflectors to a near vertical initial position. In the second scenario, which we favor, the topography of the seafloor in the footwall of the former detachment fault was, as is the case for the presently active detachment fault, controlled by mass wasting and maintained at an equilibrium slope of ~20° (Figure 15b). The rollback required to bring the 20° slope to the present-day 4° was thus only 16°, and the initial dip of the reflectors would have been about 45–60°, similar to the dip of the reflectors in the presently active detachment fault (Figure 15c). In this third hypothesis, however, it remains to be explained why the reflectors are detected up to 12 km to the south of the inferred emergence of the previously active north facing detachment fault (Sauter et al., 2013), and why the most reflective events appear to form a package between 5 km and 12 km inline distances (Figures 11 and S3 in the supporting information). In the frame of hypothesis 3 (inheritance), these characteristics would indicate very widespread and complex internal deformation in the footwall of the previous detachment fault.

We also image several subhorizontal reflectors, which occur in the shallow crust (<1 s TWT) and in the transition between crustal-type and mantle velocities in the axial domain (inline distances 7–15 km; Figure 11). The resolution of the P wave velocity model limits the identification of velocity changes corresponding to these reflectors. Observation from dredges in our study area (Sauter et al., 2013) shows that the proportion of gabbros to serpentinized peridotite is <4%, suggesting that the overall abundance of magmatic rocks is small. However, the subhorizontal reflectors could highlight isolated sill-shaped bodies of magmatic rocks similar

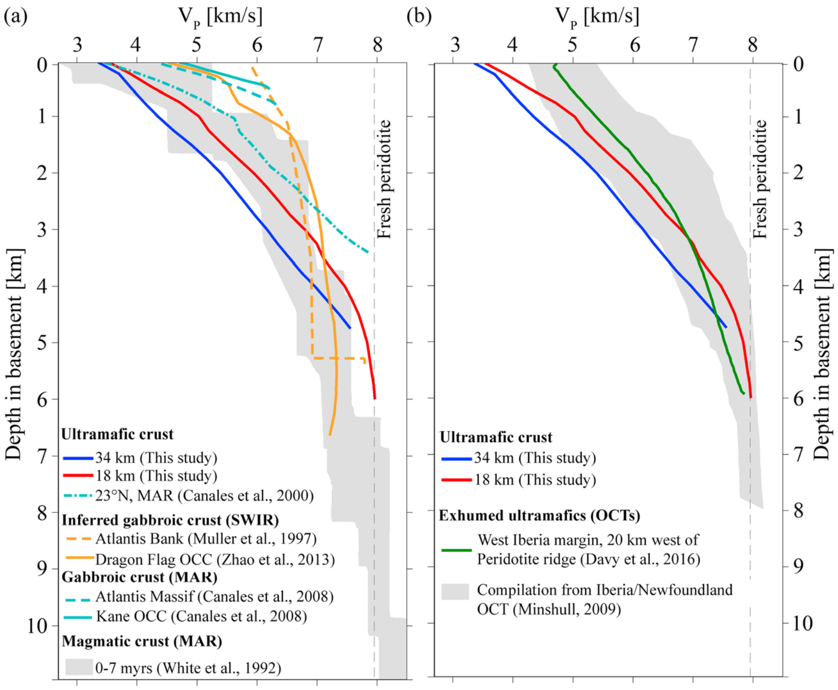

Figure 16. (a) Comparison of the *P* wave velocity profiles obtained in this study with other 1-D profiles from mid-ocean ridge OCCs where ultramafic crust is inferred (23°N, MAR) or where gabbros have been cored or inferred: Atlantis Bank, SWIR; Dragon Flag OCC, SWIR; Kane OCC, MAR. The grey area corresponds to the envelope of *P* wave velocity profiles in magmatic (0–7 Myr) reference crust in the Atlantic (White et al., 1992). (b) Comparison of the *P* wave velocity profiles obtained in this study with profiles from ocean-continent transition (OCTs) zones where exhumed serpentinized peridotites are observed or inferred (overlain by sediments) in the West Iberia margin (Davy et al., 2016). The grey area corresponds to the envelope of velocity profiles from the Western Iberia-Newfoundland magma-poor rifted margin (Minshull, 2009).

to images from other spreading centers (e.g., Canales et al., 2017; Nedimović et al., 2005). The presence of persistent melt bodies at such shallow depths is unlikely given the cold thermal regime inferred from microearthquake depths (Schlindwein & Schmid, 2016). In this context, melt is more likely to form intrusions that rapidly cool and crystallize into host ultramafic rocks (Cannat, 1993). While the crystallized sill hypothesis is the most likely for the shallow subhorizontal reflectors, the deeper family of subhorizontal reflectors could also correspond to petrological boundaries between localized domains of enhanced serpentinization and fresher peridotite. These deeper subhorizontal reflectors occur both above and below the 7.5 km/s velocity contour (Figure 13). We outline this particular velocity contour in our conceptual sketch (Figure 13) because it corresponds to the maximum velocity of olivine-rich gabbroic rocks (Miller & Christensen, 1997). Higher velocities likely correspond to weakly (<16%) serpentinized to fresh mantle. If the crystallized sill interpretation is correct, the melt reservoir would be yet deeper in the axial domain. The absence of a low-velocity anomaly resolvable on our *P* wave velocity model indicates in any case that there are no kilometer-scale bodies of melt at crustal and upper mantle depth in the axial domain.

6.3. Comparison With Tomography *P* wave Velocity Models From Other Magma-Poor Plate Divergence Domains

The two profiles extracted from our *P* wave velocity model, one at 34 km model distance (Figure 7b) and the other at 18 km, differ significantly: the geophysically defined crustal layer that we define as corresponding to *P* wave velocities <7.5 km/s (the maximum velocity for olivine-rich gabbros (Miller & Christensen, 1997)) is thicker (5 km against 4 km), and has lower velocities at any given depth, near the presently active axial detachment fault (34 km model distance), than away from this detachment (18 km model distance). We interpreted this difference as due to active extensional deformation in the hanging wall of the detachment fault. The profile extracted at 18 km model distance (Figure 16) is therefore more representative of the upper lithosphere that is passively transported off-axis as part of the Antarctic plate in this melt-starved mid-ocean ridge setting. We now compare this velocity profile with published profiles for other mid-ocean ridge OCC settings (Figure 16a) and for magma-poor OCTs (Figure 16b).

Shown in Figure 16a are the 1-D *P* wave velocity profiles for mid-ocean ridge areas where (1) gabbros have been cored or inferred (Canales et al., 2008; Muller et al., 1997; Zhao et al., 2013) and (2) ultramafic rocks are exhumed (Canales et al., 2000, 2008). The velocity patterns for profiles associated with mafic rocks indicate *P* wave velocities ≥4.5 km/s and a high velocity gradient in the upper 1 km (Canales et al., 2008). The profiles extracted from mafic areas where the *P* wave velocity is >5 km/s from 1 km in the basement with a slow velocity gradient correspond to (1) older SWIR crust (~11.5 Myr) located 26 km east of the transform valley of the Atlantis II Fracture zone and 93 km south of the ridge axis near hole 735B (Muller et al., 1997). A 3 km layer of partially serpentinized peridotite was inferred to underlie ~2 km gabbroic layer at the Atlantis Bank (Muller et al., 1997). Extensional tectonism and faulting are less apparent in this domain of older crust, hence the higher seismic velocities compared to our model which is on-axis; (2) inferred gabbroic crust in the SWIR (Zhao et al., 2013), similar in structure to tomography models from areas in the MAR where gabbros have been sampled (Canales et al., 2008) where the takeoff *P* wave velocity at the top-basement are ~4.5 km/s.

The profile associated with ultramafic basement (Mid-Atlantic Ridge at 23°N (Canales et al., 2000)) shows a linear gradient that is similar to the 1-D profile extracted from our velocity model at 34 km inline distance, although the velocity of the former is ~0.8–1 km/s higher from 1 km in the basement. This trend of higher velocities at 23°N MAR compared to our study area may be due to less internal deformation in the exhumed ultramafics or to more abundant gabbroic intrusions.

In Figure 16b, we compare our 1-D *P* wave velocity profiles with the envelope of average *P* wave velocities obtained for the Iberia-Newfoundland magma-poor rifted margin (Minshull, 2009) and with a 1-D profile extracted 20 km to the west of the Peridotite Ridge in the Western Iberia margin (Davy et al., 2016), where exhumed continental mantle with varying serpentinization rates was cored by ODP Site 637 (Boillot et al., 1987). These magma-poor rifted margins are sedimented and much older (~120 Myr (Davy et al., 2016)) compared to our study area. This probably explains why the upper ultramafic basement has higher *P* wave velocities than in our study area. The 1-D profile extracted from our velocity model at 18 km model distance is, however, within the velocity range of the OCT envelope down from 1 km in the basement. This suggests that when the enhanced fracturation-induced porosity in the upper kilometer is reduced due to increased alteration, and to the release of extensional stresses active in the ridge domain, the seismic signature of melt-starved oceanic ultramafic basement may resemble older and less fractured OCT basement.

7. Conclusions

From the analyses and interpretation of our quasi-3-D seismic reflection data and 2-D velocity modeling from ocean-bottom seismometers, our conclusions are as follows:

1. A series of bright and weak amplitude reflectors, which dip southward beneath the elevated northern wall in our study area, have been imaged and interpreted as the damage zone of the active axial detachment fault. Although the velocity model does not constrain the basement in the footwall compartment of this detachment fault due to insufficient data coverage, we observed that the velocity in the hanging wall next to the fault is 0.5–1 km/s lower than the other parts of the model at any given depth, suggesting more extensive fracturing. The series of subparallel reflectors outlining the inferred damage zone occurs in a domain that is 2–2.8 km thick, and dip 50 to 60° down to 5 km below the seafloor. This inferred damage zone could have developed as a finite system due to strain localization on a succession of individual fractures or due to distributed instantaneous deformation over a thick domain. A combination of both scenarios is also possible. Whichever is likely, we proposed that this pervasive fracturing may provide a mechanism to explain the serpentinization process on a crustal scale.
2. We have also imaged several north dipping reflective events in the hanging wall (Antarctic) plate of the axial detachment fault. For these events, we propose two alternative hypotheses: one in which the reflectors represent damage zones formed in the footwall of a previously active north dipping axial detachment fault and the other hypothesis is that the reflectors formed in response to more recent tectonic extension and incipient magmatism in the hanging wall of the presently active, south dipping axial detachment fault. We propose that flat-lying or weakly dipping discontinuous but coherent reflective events, also located in the hanging wall domain below the axial valley, may correspond to crystallized melt sills in

the velocity-defined crust and upper mantle. An alternative interpretation for the deepest events would be that they reflect contrast between locally enhanced serpentinization zones and fresher peridotite. Melt sills, if present, are volumetrically small, and there are no indications in the *P* wave tomography model for kilometer-scale bodies of partially melted material at crustal or upper mantle depth in the axial domain.

3. Crustal thickness derived from the *P* wave velocity model ranges between 4 and 5 km, where the thickest portion is observed in the hanging wall close to the active south facing axial detachment fault. The crust, on the basis of existing geological evidence and the geophysical data analyzed in this paper, is proposed to be composed mainly of variably serpentinized peridotite.
4. Vertical velocity profiles extracted from out *P* wave velocity model display nearly linear velocity to depth gradients, similar to those observed over ultramafic seafloor at the 23°N MAR (Canales et al., 2000). Velocity values deeper than 1 km into the basement, however, are higher at 23°N MAR, which may be due to less internal deformation in the exhumed ultramafics and to more abundant gabbroic intrusions. Our velocity profiles also show similarities with the average *P* wave velocity structure of OCT basement from the Iberia-Newfoundland magma-poor rifted margin (Minshull, 2009).

Acknowledgments
We thank the Flotte Océanographique Française (FOF) for funding the SISMOSMOOTH cruise and Institut Polaire Français Paul-Émile Victor (IPEV) for the cruise onboard French research vessel *Marion-Dufresne* (technical team led by Hélène Leau). CNRS-INSU Tellus provided support for the cruise (funding before and after the cruise, and SYSTER program) and also a part of the ANR Rift2Ridge NT09-48546. We also thank Captain Thierry Dudouit (CMO-CGM) and the crew of the R/V *Marion-Dufresne*: Erwan Nedelec and Jean-Charles Guedes (Genavir) for the seismic deployment. This manuscript benefited from incisive reviews from Juan-Pablo Canales and an anonymous reviewer. We thank them. Data discussed here would be available on demand at SISMER (www.ifremer.fr/sismer/). This is IPGP contribution number 3885.

References

Abma, R., & Kabir, N. (2005). Comparisons of interpolation methods. *The Leading Edge*, *24*(4), 984–989. https://doi.org/10.1190/1.2112371

Agrinier, P., & Cannat, M. (1997). Oxygen-isotope constraints on serpentinization processes in ultramafic rocks from the Mid-Atlantic Ridge (23°N). In J. A. Karson, et al. (Eds.), *Proceedings of the Ocean Drilling Program, Scientific Results* (Vol. 153, pp. 381–388). https://doi.org/10.2973/odp.proc.sr.153.033.1997

Al-Chalabi, M. (1994). Seismic velocities – a critique. *First Break*, *12*(12), 569–596. https://doi.org/10.3997/1365-2397.1994.36

Andréani, M., Mevel, C., Boullier, A.-M., & Escartín, J. (2007). Dynamic control on serpentine crystallization in veins: Constraints on hydration processes in oceanic peridotites. *Geochemistry, Geophysics, Geosystems*, *8*, Q02012. https://doi.org/10.1029/2006/GC001373

Andréani, M., Ildefonse, B., Delacour, A., Escartín, J., Godard, M., Dyment, J., … Fouquet, Y. (2014). Tectonic structure, lithology and hydrothermal signature of the Rainbow massif (Mid-Atlantic Ridge 36°14′N). *Geochemistry, Geophysics, Geosystems*, *15*, 3543–3571. https://doi.org/10.1002/2014GC005269

Bansal, R., & Imhof, M. G. (2005). Diffraction enhancement in prestack seismic data. *Geophysics*, *70*(3), V73–V79. https://doi.org/10.1190/1.1926577

Blackman, D. K., & Collins, J. A. (2010). Lower crustal variability and the crust/mantle transition at the Atlantis Massif oceanic core complex. *Geophysical Research Letters*, *37*, L24303. https://doi.org/10.1029/2010GL045165

Boillot, G., Winterer, E., Meyer, A. W. & Shipboard Scientific Party (1987). Introduction, objectives, and principal results: Ocean Drilling Program Leg 103, West Galicia Margin. In G. Boillot, et al. (Eds.). *Proceedings of the Ocean Drilling Program, Initial Reports* (Vol. 103, pp. 3–17). https://doi.org/10.2973/odp.proc.ir.103.101.1987

Bonatti, E. (1976). Serpentine protrusions in the oceanic crust. *Earth and Planetary Science Letters*, *32*, 107–113. https://doi.org/10.1016/0012-821X(76)90048-0

Buck, W. R. (1988). Flexural rotation of normal faults. *Tectonics*, *7*(5), 959–973. https://doi.org/10.1029/TC007i005p00959

Buck, W. R., Lavier, L. L., & Poliakov, A. N. B. (2005). Modes of faulting at mid-ocean ridges. *Nature*, *434*, 719–723. https://doi.org/10.1038/nature03358

Canales, J. P., Collins, J. A., Escartín, J., & Detrick, R. S. (2000). Seismic structure across the rift valley of the Mid-Atlantic Ridge at 23°20′N (MARK area): Implications for crustal accretion processes at slow-spreading ridges. *Journal of Geophysical Research*, *105*, 28,411–28,425. https://doi.org/10.1029/2000JB900301

Canales, J. P., Tucholke, B. E., Xu, M., Collins, J. A., & Dubois, D. L. (2008). Seismic evidence for large-scale compositional heterogeneity of oceanic core complexes. *Geochemistry, Geophysics, Geosystems*, *9*, Q08002. https://doi.org/10.1029/2008GC002009

Canales, J. P., Dunn, R. A., Arai, R., & Sohn, R. A. (2017). Seismic imaging of magma sills beneath an ultramafic-hosted hydrothermal system. *Geology*, *45*, 447–450. https://doi.org/10.1130/G38795.1

Cann, J. R., Blackman, D. K., Smith, D. K., McAllister, E., Janssen, B., Mello, S., … Escartín, J. (1997). Corrugated slip surfaces formed at ridge-transform intersections on the Mid-Atlantic Ridge. *Nature*, *385*, 329–332. https://doi.org/10.1038/385329a0

Cannat, M. (1993). Emplacement of mantle rocks in the seafloor at mid-ocean ridges. *Journal of Geophysical Research*, *98*(B3), 4163–4172. https://doi.org/10.1029/92JB02221

Cannat, M., Mével, C., Maia, M., Deplus, C., Durand, C., Gente, P., … Reynolds, J. (1995). Thin crust, ultramafic exposures, and rugged faulting patterns at the Mid-Atlantic Ridge (22°-24°N). *Geology*, *23*(1), 49–52. https://doi.org/10.1130/0091-7613(1995)023%3C0049:TCUEAR%3E2.3.CO;2

Cannat, M., Lagabrielle, Y., Bougault, H., Casey, J., deCoutures, N., Dmitriev, L., & Fouquet, Y. (1997). Ultramafic and gabbroic exposures at the Mid-Atantic Ridge: geological mapping in the 15°N region. *Tectonophysics*, *279*, 193–213. https://doi.org/10.1016/S0040-1951(97)00113-3

Cannat, M., Rommevaux-Jestin, C., Sauter, D., Deplus, C., & Mendel, V. (1999). Formation of the axial relief at the very slow spreading Southwest Indian Ridge (49° to 69°E). *Journal of Geophysical Research*, *104*, 22,825–22,843. https://doi.org/10.1029/1999JB900195

Cannat, M., Sauter, D., Mendel, V., Ruellan, E., Okino, K., Escartín, J., … Baala, M. (2006). Modes of seafloor generation at a melt-poor ultraslow-spreading ridge. *Geology*, *37*(7), 605–608. https://doi.org/10.1130/G22486.1

Cannat, M., Sauter, D., Bezos, A., Meyzen, C., Humler, E., & Le Rigoleur, M. (2008). Spreading rate, spreading obliquity, and melt supply at the ultraslow spreading Southwest Indian Ridge. *Geochemistry, Geophysics, Geosystems*, *9*, Q04002. https://doi.org/10.1029/2007GC001676

Cannat, M., Fontaine, F., & Escartín, J. (2010). Serpentinization and associated hydrogen and methane fluxes at slow spreading ridges. In P. A. Rona, et al. (Eds.), *Diversity of hydrothermal systems on slow spreading ocean ridges* (pp. 241–264). Washington, DC: American Geophysical Union. https://doi.org/10.1029/2008GM000760

Cannat, M., Sauter, D., & Rouméjon, S. (2012). Formation of an ultramafic seafloor at the Southwest Indian Ridge 62°–65°E: internal structure of detachment faults and sparse volcanism documented by sidescan sonar and dredges. Abstract OS11E-03 Presented at the 2012 AGU Fall Meeting, San Francisco, CA, 3–7 Dec.

Cannat, M., Mangeney, A., Ondréas, H., Fouquet, Y., & Normand, A. (2013). High-resolution bathymetry reveals contrasting landslide activity shaping the walls of the Mid-Atlantic Ridge axial valley. *Geochemistry, Geophysics, Geosystems*, *14*, 996–1011. https://doi.org/10.1002/ggge.20056

Cannat, M., Agrinier, P., Bickert, M., Brunelli, D., Hamelin, D., Lecoeuvre, A., … Assaoui, M. (2017). Mid ocean ridge processes at very low melt supply: submersible exploration of smooth ultramafic seafloor at the Southwest Indian Ridge, 64°E. Abstract T32C-01 Presented at the 2017 AGU Fall Meeting, New Orleans, LA, 11–15 Dec.

Christensen, N. I. (1972). The abundance of serpentinites in the oceanic crust. *Journal of Geology*, *80*, 709–719. https://doi.org/10.1086/627796

Christensen, N. I. (2004). Serpentinites, peridotites and seismology. *International Geology Review*, *46*, 795–816. https://doi.org/10.2747/0020-6814.46.9.795

Daley, T. M., Nihei, K. T., Myer, L. R., Majer, E. L., Queen, J. H., Fortuna, M., & Murphy, J. (2002). Numerical modeling of scattering from discrete fracture zones in a San Juan Gas Basin Reservoir. Paper presented at the 72nd Society of Exploration Geophysicists Annual International Meeting (pp. 109–112). Salt Lake City, UT.

Davies, E. R. (1992). The relative effects of median and mean filters on noisy signals. *Journal of Modern Optics*, *39*(1), 103–113. https://doi.org/10.1080/713823346

Davy, R. G., Minshull, T. A., Bayrakci, G., Bull, J. M., Klaeschen, D., Papenberg, C., … Zelt, C. A. (2016). Continental hyperextension, mantle exhumation, and thin oceanic crust at the continent-ocean transition, West Iberia: new insights from wide-angle seismic. *Journal of Geophysical Research: Solid Earth*, *121*, 3177–3188. https://doi.org/10.1002/2016JB012825

deMartin, B. J., Sohn, R. A., Canales, J. P., & Humphris, S. E. (2007). Kinematics and geometry of active faulting beneath the Trans-Atlantic Geotraverse (TAG) hydrothermal field on the Mid-Atlantic Ridge. *Geology*, *35*(8), 711–714. https://doi.org/10.1130/G23718A.1

Detrick, R., Collins, J., & Swift, S. (1994). In situ evidence for the nature of the seismic layer 2/3 boundary in oceanic crust. *Nature*, *370*, 288–290. https://doi.org/10.1038/370288a0

Dick, H. J. B., Bryan, W. B., & Thompson, G. (1981). Low-angle faulting and steady-state emplacement of plutonic rocks at ridge-transform intersections. *Eos, Transactions of the American Geophysical Union*, *62*, 406.

Dick, H. J. B., Lin, J., & Schouten, H. (2003). An ultraslow-spreading class of ocean ridge. *Nature*, *426*, 405–412. https://doi.org/10.1038/nature02128

Dick, H. J. B., Tivey, M. A., & Tucholke, B. E. (2008). Plutonic foundation of a slow-spreading ridge segment: Oceanic core complex at Kane Megamullion, 23°30′N, 45°20′W. *Geochemistry, Geophysics, Geosystems*, *9*, Q05014. https://doi.org/10.1029/2007GC001645

Escartín, J., Mével, C., MacLeod, C. J., & McCaig, A. M. (2003). Constraints on deformation conditions and the origin of oceanic detachments: The Mid-Atlantic Ridge core complex at 15°45′N. *Geochemistry, Geophysics, Geosystems*, *4*(8), 1067. https://doi.org/10.1029/2002GC000472

Escartín, J., Smith, D. K., Cann, J., Schouten, H., Langmuir, C. H., & Escrig, S. (2008). Central role of detachment faults in accretion of slow-spreading oceanic lithosphere. *Nature*, *455*(9), 790–794. https://doi.org/10.1038/nature07333

Escartín, J., Mével, C., Petersen, S., Bonnemains, D., Cannat, M., Andréani, M., … Garcia, R. (2017). Tectonic structure, evolution, and the nature of oceanic core complexes and their detachment fault zones (13°20′N and 13°30′N, Mid Atlantic Ridge). *Geochemistry, Geophysics, Geosystems*, *18*, 1451–1482. https://doi.org/10.1002/2016GC006775

Etris, E. L., Crabtree, N. J., & Dewar, J. (2001). True depth conversion: more than a pretty picture. *CSEG Recorder*, *26*(9), 11–22.

Ferber, R., Caproili, P., & West, L. (2013). L1 pseudo-V_Z estimation and deghosting of single-component marine towed-streamer data. *Geophysics*, *78*(2), WA21–WA26. https://doi.org/10.1190/geo2012-0293.1

Früh-Green, G. L., Connolly, J. A. D., Plas, A., Kelley, D. S., & Grobéty, B. (2004). Serpentinization of oceanic peridotites: Implications for geochemical cycles and biological activity. *Geophysical Monograph Series*, *144*, 119–136. https://doi.org/10.1029/144GM08

Garcés, M., & Gee, J. S. (2007). Paleomagnetic evidence of large footwall rotations associated with low-angle faults at the Mid-Atlantic Ridge. *Geology*, *35*(3), 279–282. https://doi.org/10.1130/G23165A.1

Gudmundsson, A., Simmenes, T. H., Larsen, B., & Philip, S. L. (2010). Effects of internal structure and local stresses on fracture propagation, deflection, and arrest in fault zones. *Journal of Structural Geology*, *32*, 1643–1655. https://doi.org/10.1016/j.jsg.2009.08.013

Gudmundsson, A., De Guidi, G., & Scudero, S. (2013). Length-displacement scaling and fault growth. *Tectonophysics*, *608*, 1298–1309. https://doi.org/10.1016/j.tecto.2013.06.012

Karson, J. A. (1990). Seafloor spreading on the Mid-Atlantic Ridge: Implications for the structure of ophiolites and oceanic lithosphere produced in slow-spreading environments. In J. Malpas, et al. (Eds.), *Proceedings of the Symposium TROODOS 1987* (pp. 547–555). Nicosia Cyprus: Geological Survey Department.

Karson, J. A., Thompson, G., Humphris, S. E., Edmond, J. M., Bryan, W. B., Brown, J. R., … Sulanowska, M. M. (1987). Along-axis variations in seafloor spreading in the MARK area. *Nature*, *328*(20), 681–685. https://doi.org/10.1038/328681a0

Korenaga, J., Holbrook, W. S., Kent, G. M., Kelemen, P. B., Detrick, R. S., Larsen, H. C., … Dahl-Jensen, T. (2000). Crustal structure of the southeast Greenland margin from joint refraction and reflection seismic tomography. *Journal of Geophysical Research*, *105*, 21,591–21,614. https://doi.org/10.1029/2000JB900188

Lavier, L. L., Buck, W. R., & Poliakov, A. N. B. (1999). Self-consistent rolling-hinge model for the evolution of large-offset low-angle normal faults. *Geology*, *27*(12), 1127–1130. https://doi.org/10.1130/0091-7613(1999)027%3C1127:SCRHMF%3E2.3.CO;2

Leroy, S., Cannat, M., Momoh, E., Singh, S., Watremez, L., Sauter, D., … Wang, S. (2015). Anatomy of ultra-slow spreading Southwest Indian Ridge: The 2014 SISMOSMOOTH cruise. Abstract V21A-3027 Paper presented at the 2015 AGU, San Francisco, CA, 14–18 Dec.

Liner, C. L. (1990). General theory and comparative anatomy of dip moveout. *Geophysics*, *55*(5), 595–607. https://doi.org/10.1190/1.1442871

Liner, C. L. (2004). *Elements of 3D seismology* (2nd ed.). Tulsa, OK: PennWell. https://doi.org/10.1190/1.9781560803386

Lister, C. R. B. (1974). On the penetration of water into hot rock. *Geophysical Journal of the Royal Astronomical Society*, *39*, 465–509.

Lu, L. (1985). Application of local slant stack to trace interpolation. Paper presented at the Society of Exploration Geophysicists Annual International Meeting (Vol. *4*, pp. 560–562). https://doi.org/10.1191/1.1892818

MacLeod, C. J., Escartín, J., Banerji, D., Banks, G. J., Gleeson, M., Irving, D. H. B., … Smith, D. K. (2002). Direct evidence for oceanic detachment faulting: The Mid-Atlantic Ridge, 15°45′N. *Geology*, *30*(10), 879–882. https://doi.org/10.1130/0091-7613(2002)030%3C0879:DGEFOD%3E2.0.CO;2

MacLeod, C. J., Searle, R. C., Murton, B. J., Casey, J. F., Mallows, C., Unsworth, S. C., … Harris, M. (2009). Life cycle of oceanic core complexes. *Earth and Planetary Science Letters*, *287*(3–4), 333–344. https://doi.org/10.1016/j.epsl.2009.08.016

Mével, C., Cannat, M., Gente, P., Marion, E., Auzende, J.-M., & Karson, J. A. (1991). Emplacement of deep mantle rocks on the west Medial Valley Wall of the MARK area. *Tectonophysics*, *190*, 31–53. https://doi.org/10.1016/0040-1951(91)90353-T

Miller, D. J., & Christensen, N. I. (1997). Seismic velocities of lower crustal and upper mantle rocks from the slow spreading Mid-Atlantic Ridge, south of the Kane transform zone (MARK). In J. A. Karson, M. Cannat, D. J. Miller, D. Elthon (Eds.). *Proceeding of the Ocean Drilling Program, Scientific Results*, 153, 437–454. https://doi.org/10.2973/odp.proc.sr.153.043.1997

Minshull, T. A. (2009). Geophysical characterization of the ocean-continent transition at magma-poor rifted margins. *Comptes Rendus Geoscience*, *341*(5), 382–393. https://doi.org/10.1016/j.crte.2008.09.003

Minshull, T. A., & White, R. S. (1996). Thin crust on the flanks of the slow-spreading Southwest Indian Ridge. *Geophysical Journal International*, *125*, 139–148. https://doi.org/10.1111/j.1365-246X.1996.tb06541.x

Minshull, T. A., Muller, M. R., & White, R. S. (2006). Crustal structure of the Southwest Indian Ridge at 66°E: Seismic constraints. *Geophysical Journal International*, *166*, 135–147. https://doi.org/10.1111/j.1365-246X.2006.03001.x

Momoh, E., Halliday, D., Ferber, R., & Singh, S. (2015). Pseudo-V_z deghosting of deep-tow seismic data and implications for low-frequency signal estimation. Paper presented at the Society of Exploration Geophysicists Annual International Meeting (pp. 4525–4529). https://doi.org/10.1190/segam2015-5901595.1

Momoh, E., Halliday, D., Ferber, R., & Singh, S. (2016). Low-frequency signal enhancement by pseudo-V_z deghosting. *First Break*, *34*(3), 35–43. https://doi.org/10.3997/1365-2397.2016003

Morris, A., Gee, J. S., Pressling, N., John, B. E., MacLeod, C. J., Grimes, C. B., & Searle, R. C. (2009). Footwall rotation in an oceanic core complex quantified using reoriented Integrated Ocean Drilling Program core samples. *Earth and Planetary Science Letters*, *287*, 217–228. https://doi.org/10.1016/j.epsl.2009.08.007

Muller, M. R., Robinson, C. J., Minshull, T. A., White, R. S., & Bickle, M. J. (1997). Thin crust beneath ocean drilling program borehole 735B at the Southwest Indian Ridge? *Earth and Planetary Science Letters*, *148*, 93–107. https://doi.org/10.1016/S0012-821X(97)00030-7

Muller, M. R., Minshull, T. A., & White, R. S. (1999). Segmentation and melt supply at the Southwest Indian Ridge. *Geology*, *27*, 867–870. https://doi.org/10.1130/0091-7613(1999)027%3C0867:SAMSAT%3E2.3.CO;2

Nedimović, M. R., Carbotte, S. M., Harding, A. J., Detrick, R. S., Canales, J. P., Diebold, J. B., … Babcock, J. (2005). Frozen magma lenses below the oceanic crust. *Nature*, *436*, 1149–1152. https://doi.org/10.1038/nature03944

Parnell-Turner, R., Sohn, R. A., Pierce, C., Reston, T. J., MacLeod, C. J., Searle, R. C., & Simão, N. M. (2017). Oceanic detachment faults generate compression in extension. *Geology*, *45*(10), 923–926. https://doi.org/10.1130/G39232.1

Patriat, P., & Segoufin, J. (1988). Reconstruction of the central Indian Ocean. *Tectonophysics*, *155*, 211–234. https://doi.org/10.1016/0040-1951(88)90267-3

Picazo, S., Cannat, M., Delacour, A., Escartín, J., Rouméjon, S., & Silantyev, S. (2012). Deformation associated with the denudation of mantle-derived rocks at the Mid-Atlantic Ridge 13°–15°N: The role of magmatic injections and hydrothermal alteration. *Geochemistry, Geophysics, Geosystems*, *13*, Q04G09. https://doi.org/10.1029/2012GC004121

Planert, L., Flueh, E. R., & Reston, T. J. (2009). Along- and across-axis variations in crustal thickness and structure at the Mid-Atlantic Ridge at 5°S obtained from wide-angle seismic tomography: Implications for ridge segmentation. *Journal of Geophysical Research*, *114*, B09102. https://doi.org/10.1029/2008JB006103

Planert, L., Flueh, E. R., Tilmann, F., Grevemeyer, I., & Reston, T. J. (2010). Crustal structure of a rifted oceanic core complex and its conjugate side at the MAR at 5°S: implications for melt extraction during detachment faulting and core complex formation. *Geophysical Journal International*, *181*, 113–126. https://doi.org/10.1111/j.1365-246X.201004504.x

Plümper, O., Røyne, A., Margrasó, A., & Jamveit, B. (2012). The interface-scale mechanism of reaction-induced fracturing during serpentinization. *Geology*, *40*(12), 1103–1106. https://doi.org/10.1130/G33390.1

Reston, T. J., & Ranero, C. R. (2011). The 3D geometry of detachment faulting at mid-ocean ridges. *Geochemistry, Geophysics, Geosystems*, *12*, Q0AG05. https://doi.org/10.1029/2011GC003666

Robinson, E. A. (1967). Predictive decomposition of time series with application to seismic exploration. *Geophysics*, *32*(3), 418–484. https://doi.org/10.1190/1.1439873

Robinson, E. A. (1981). Predictive deconvolution. In A. A. Fitch (Ed.), *Developments in geophysical exploration methods* (pp. 77–106). Dordrecht: Springer. https://doi.org/10.1007/978-94-009-8105-8

Rouméjon, S., & Cannat, M. (2014). Serpentinization of mantle-derived peridotites at mid-ocean ridges: Mesh texture development in the context of tectonic exhumation. *Geochemistry, Geophysics, Geosystems*, *15*, 2354–2379. https://doi.org/10.1002/2013GC005148

Rouméjon, S., Cannat, M., Agrinier, P., Godard, M., & Andréani, M. (2015). Serpentinization and fluid pathways in tectonically exhumed peridotites from the Southwest Indian ridge. *Journal of Petrology*, *56*(4), 703–734. https://doi.org/10.1093/petrology/egv014

Saenger, E., Shapiro, S., & Kruger, O. (2002). Simulation of diffractions by single cracks. Paper presented at the 72nd Society of Exploration Geophysicists Annual International Meeting (pp. 2007–2010). https://doi.org/10.1190/1.1817092

Sato, T., Okino, K., & Kumahai, H. (2009). Magnetic structure of an oceanic core complex at the southernmost Central Indian Ridge: Analysis of shipboard and deep sea three-component magnetometer data. *Geochemistry, Geophysics, Geosystems*, *10*, Q06003. https://doi.org/10.1029/2008GC002267

Sauter, D., Cannat, M., Rouméjon, S., Andréani, M., Birot, D., Bronner, A., … Searle, R. C. (2013). Continuous exhumation of mantle-derived rocks at the Southwest Indian Ridge for 11 million years. *Nature Geoscience*, *6*, 314–320. https://doi.org/10.1038/NGEO1771

Schlindwein, V., & Schmid, F. (2016). Mid-ocean-ridge seismicity reveals extreme types of ocean lithosphere. *Nature*, *535*, 276–279. https://doi.org/10.1038/nature18277

Schneider, W. A. (1978). Integral formulation for migration in two and three dimensions. *Geophysics*, *43*(1), 49–76. https://doi.org/10.1190/1.1440828.4

Schouten, H., Smith, D. K., Cann, J. R., & Escartín, J. (2010). Tectonic versus magmatic extension in the presence of core complexes at slow spreading ridges from a visualization of faulted seafloor topography. *Geology*, *38*(7), 615–618. https://doi.org/10.1130/G30803.1

Seyler, M., Cannat, L., & Mével, C. (2003). Evidence for major-element heterogeneity in the mantle source of abyssal peridotites from the Southwest Indian Ridge (52° to 68°E). *Geochemistry, Geophysics, Geosystems*, *4*(2), 9101. https://doi.org/10.1029/2002GC000305

Smith, D. K., Cann, J. R., & Escartín, J. (2006). Widespread active detachment faulting and core complex formation near 13°N on the Mid-Atlantic Ridge. *Nature*, *442*, 440–443. https://doi.org/10.1038/nature04950

Smith, D. K., Schouten, H., Dick, H. J. B., Cann, J. R., Salters, V., Marschall, H. R., … Curry, S. (2014). Development and evolution of detachment faulting along 50 km of the Mid-Atlantic Ridge near 16.5N. *Geochemistry, Geophysics, Geosystems*, *15*, 4692–4711. https://doi.org/10.1002/2014GC005563

Spudich, P., & Orcutt, J. (1980). A new look at the seismic velocity structure of the oceanic crust. *Reviews of Geophysics*, *18*, 627–645. https://doi.org/10.1029/RG018i003p00627

Sun, J. (1998). On the limited aperture migration in two dimensions. *Geophysics*, *64*(3), 984–994. https://doi.org/10.1190/1.1444409
Sun, S., & Bancroft, J. C. (2001). How much does the migration aperture actually contribute to the migration result? Paper presented at the Society of Exploration Geophysicists Annual International Meeting (pp. 973–976). https://doi.org/10.1190/1.1816802
Thurber, C. H. (1983). Earthquake locations and three-dimensional crustal structure in the Coyote Lake area, central California. *Journal of Geophysical Research*, *88*, 8226–8236. https://doi.org/10.1029/JB088iB10p08226
Toomey, D. R., Solomon, S. C., Purdy, G. M., & Murray, M. H. (1988). Microearthquakes beneath the median valley of the Mid-Atlantic Ridge near 23°N: Tomography and tectonics. *Journal of Geophysical Research*, *93*, 9093–9112. https://doi.org/10.1029/JB093iB08p09093
Tucholke, B. E., Fujioka, K., Ishihara, T., Hirth, G., & Kinoshita, M. (2001). Submersible study of an oceanic megamullion in central North Atlantic. *Journal of Geophysical Research*, *106*, 145–161. https://doi.org/10.1029/2001JB000373
Tucholke, B. E., Behn, M. D., Buck, W. R., & Lin, J. (2008). Role of melt supply in oceanic detachment faulting and formation of megamullions. *Geology*, *36*(6), 455–458. https://doi.org/10.1130/G24639A.1
White, R. S., McKenzie, D., & O'Nions, R. K. (1992). Oceanic crustal thickness from seismic measurements and rare element inversions. *Journal of Geophysical Research*, *97*(B13), 19,683–19,715. https://doi.org/10.1029/92JB01749
Wolfe, C. J., Purdy, G., Toomey, D., & Solomon, S. (1995). Microearthquake characteristics and crustal velocity structure at 29°N on the Mid-Atlantic Ridge: The architecture of a slow spreading segment. *Journal of Geophysical Research*, *100*(B12), 24,449–24,472. https://doi.org/10.1029/95JB02399
Yilmaz, Ö. (2001). Seismic data analyses, processing, inversion and interpretation of seismic data (Vols. *1 and 2*, pp. 1–2065). Tulsa, OK: Society of Exploration Geophysicists. https://doi.org/10.1190/1.9781560801580
Zhang, J., & Toksöz, M. N. (1998). Nonlinear refraction traveltime tomography. *Geophysics*, *63*, 1726–1737. https://doi.org/10.1190/1.1444468
Zhao, M., Qui, X., Li, J., Sauter, D., Ruan, A., Chen, J., … Niu, X. (2013). Three-dimensional seismic structure of the Dragon Flag oceanic core complex at the ultraslow spreading Southwest Indian Ridge (49°39′E). *Geochemistry, Geophysics, Geosystems*, *14*, 4544–4563. https://doi.org/10.1002/ggge.20264

Erratum

In the originally published version of this article, Table 1 contained an error: The first entry under OBS profiles titled "Air gun volume" should have appeared as 111.27 L. Table 2 was incorrectly typeset resulting in a lack of organization of the data. The data appearing below "Prestack processing" should have appeared as: "Resample to 4 ms after antialias filter, 125 Hz cutoff." The errors have been corrected, and this version may be considered the authoritative version of record.